When to Learn and When to Forget: NMDA Normalization in Hippocampal Neurons - Activity-Dependent, Temporal and Spatial Properties

by

Safa Sadeghpour
B.S. Neuroscience and Cybernetics
UCLA, 1998

SUBMITTED TO THE DEPARTMENT OF HEALTH SCIENCE AND TECHNOLOGY IN PARTIAL FULFILLMENT OF THE REQUIREMENTS FOR THE DEGREE OF

PHILOSOPHIAE DOCTOR (Ph.D.) IN HEALTH SCIENCES AND TECHNOLOGY
(BRAIN AND COGNITIVE SCIENCES)
AT THE
MASSACHUSETTS INSTITUTE OF TECHNOLOGY

AUGUST 2005 [June 2007]

Signature of Author:

Department of Health Sciences and Technology (Brain and Cognitive Sciences)
August 25, 2005

Certified by:

Guosong Liu, Ph.D.
Associate Professor of Brain and Cognitive Sciences
Thesis Supervisor

Accepted by:

Martha L. Gray, Ph.D.
Edward Hood Taplin Professor of Medical and Electrical Engineering
Director, Harvard-MIT Division of Health Sciences and Technology

Summary

Synaptic plasticity is the substrate of a vast variety of learning mechanisms. However, the molecular pathways and physiological patterns that regulate it are poorly understood.

In the first part of this thesis, we focus on the physiological determinants of pre-synaptic plasticity. We find that a complete blockade of activity succeeds in inducing only a transient enhancement of plasticity. A permanent enhancement of synaptic plasticity is achieved by selectively reducing the NMDA-R mediated Ca^{2+} flux associated with uncorrelated activity, via adjustment of the voltage-dependent Mg^{2+} block of NMDA receptors. NR2B-containing NMDARs are up-regulated by this treatment, and this is found to be an important contributor to plasticity enhancement. Thus, the quality, but not the quantity, of activity is the important parameter to manipulate to obtain a permanent enhancement of intrinsic plasticity.

In the second part, we study the relationship between activity patterns and post-synaptic NMDA-R regulation by using high-precision iontophoresis. We identified a new homeostatic mechanism of NMDA-R regulation which we have thus termed "NMDA Normalization" to differentiate it from prior uses of "NMDA homeostasis." Through this novel Ca++ dependent mechanism, we show that the neuron, by opposing NMDA-R functional expression counter to activity changes, causes the average charge transfer through NMDA-Rs to remain constant. We elucidate the activity-dependent, temporal, and spatial characteristics of this process.

We propose an explanatory hypothesis. The reduction of uncorrelated activity used in the first part reduced the NMDA-R mediated average charge transfer. Through normalization, the cell increased functional NMDA-R expression to normalize NMDA-R mediated average charge transfer. However, when a burst of activity arrives in this new condition, in which an identical burst of glutamate release and depolarization now meets a larger number of very weakly activated NMDA-Rs, it is able to induce a disproportionately larger peak Ca++ flux. This increase in the maximal Ca++ flux, due to the combination of reduction of uncorrelated activity and NMDA-R normalization, is responsible in great part for the enhancement of synaptic plasticity.

Our findings propose a clear strategy for the development of compounds to restore, and potentially enhance, synaptic plasticity, and thus with likelihood learning and memory.

Activity-Dependent Regulation

of Pre-synaptic Plasticity through

Modulation of NMDA-R Functional Expression

Introduction

Synaptic plasticity is known to be essential for achieving the proper organization of neural circuits during early development and for the storage of information in later stages. However, the regulation of intrinsic plasticity of synapses under physiological conditions is not fully understood. Prior work on the regulation of cortical map plasticity during development provides important clues. Pioneering studies by Hubel and Wiesel (1963) demonstrate that there exists a critical period during which depriving an eye of visual input dramatically alters thalamo-cortical projections in favor of the other eye. Since then, many other experiments have been carried out to determine the mechanisms that engender this critical period during which reorganization of cortical connections is possible (rev. Katz & Shatz, 1996; Shatz & Stryker, 1988; Stryker & Harris, 1986). We now know that, in the visual system, a developmental increase of neural input and activity leads to the eventual down-regulation of the malleability of cortical representations. In contrast, reducing input activity via dark rearing prolongs the critical period for ocular dominance plasticity (Fagiolini, Pizzorusso, Berardi, Domenici, & Maffei, 1994; Timney, Mitchell, & Giffin, 1978). Similar relationships between activity and circuitry reorganization have since been established in somatosensory (Fox, 1992) and auditory (Chang & Merzenich, 2003) cortices as well. Thus, as a general trend, changes in ongoing neural activity correlate inversely with topographic map plasticity in these hierarchically early sensory cortices.

As the plasticity of individual synapses is essential for reorganization of cortical connections (revs. Bear, 2003; Buonomano & Merzenich, 1998), it is possible that the

above relationship also holds between activity and synaptic plasticity. While it is well known that brief bursts of activity (~seconds/minutes; ~10^2 APs) modify the efficacy of synaptic connections and their plasticity in neuronal circuits, the long-term effect of neural activity (> hours-lifetime; ~10^3 - 10^8 APs) on synaptic and cellular plasticity remains elusive (Abraham & Bear, 1996).

In this study we first set out to determine the elementary relationship between the network's level of neural activity and the plasticity of its individual synapses. To achieve this goal we needed to be able to modify neural activity and then directly monitor the plasticity of large numbers of synapses. To accomplish this we employed a reduced experimental preparation of hippocampal neurons in culture where we could, in a clear-cut fashion, both control the activity and monitor the functional state and plasticity of large numbers of presynaptic terminals. We have used this system to answer these initial questions: Do neural activity and inhibition play a critical role in the plasticity of hippocampal synapses, as they do in early sensory cortices? If so, is the magnitude of plasticity tuned continuously and reversibly according to the level of activity? What is the signalling pathway that relates the quantity/quality of activity to synaptic plasticity? For this last question, we wished to distinguish between membrane depolarization and Ca^{2+} flux as potential secondary messengers of importance, and determine whether it is the integral (quantity) or precise spatio-temporal pattern (quality) of this intermediary that is the critical regulator. Finally, we explored the synaptic properties that might be essential for a synapse to be and remain plastic.

We found that the neural circuit contained large numbers of synaptic terminals with low probability of release, thus constituting a large reserve pool of "quiet" connections. The plasticity of these terminals was enhanced following the reduction of neural activity. We identified Ca^{2+} flux through NMDA and voltage gated calcium channels (VGCCs) as the messenger that regulates the plasticity of synapses and release of BDNF as a mediator of presynaptic potentiation. However, we found that uniform reduction of Ca^{2+} flux failed to induce long-lasting enhancement of synaptic plasticity, suggesting a complex role for Ca^{2+} flux in the regulation of presynaptic plasticity. Interestingly, selective attenuation of NMDAR-mediated Ca^{2+} flux during uncorrelated activity obtained by adjusting the voltage-dependent Mg^{2+} blockade resulted in a permanent conversion of synapses to a plastic state. We deduce that the inverse and reversible relationship between the neural activity and synaptic plasticity, mediated through precise patterning of Ca^{2+} fluxes, may represent an elementary property of hippocampal circuits.

Results

The majority of presynaptic terminals exhibit a low probability of release

To understand precisely the mechanisms regulating hippocampal synaptic plasticity, the physiological properties of individual synapses had to be studied. First, we determined the distribution of release probability (Pr) of single CNS synapses by counting the number of presynaptic vesicles turned over by a fixed number of action potentials using activity-dependent FM dye uptake as a marker (Murthy, Sejnowski, & Stevens, 1997; Murthy & Stevens, 1998; Ryan, Smith, & Reuter, 1996). Action potentials triggered synaptic vesicle exocytosis and endocytosis, which labeled exocytosed vesicles with FM 1-43 (see Figure 1A for loading protocol). Figure 1Ba shows an image containing several FM-dye puncta following FM 1-43 loading for 30 action potentials (APs). The majority of FM dye spots were destained as a result of the second stimulation set (480 AP@ 2 Hz, Figure 1Bb). We calculated the total amount of releasable fluorescence at each bouton (ΔF) from the difference between initial (Figure 1Ba) and final fluorescence (Figure 1Bb). From this value, we inferred the number of exocytosed synaptic vesicles per individual terminal by calculating the ratio $\Delta F/F_Q$, where F_Q is the estimated releasable fluorescence of a single synaptic vesicle. Thus, the Pr of individual terminals was calculated by $Pr = \Delta F/(N_{AP} \times F_Q)$, where N_{AP} is the number of APs applied during loading. If one can detect a ΔF as small as F_Q, this permits one to monitor terminals with extremely low Pr. We determined that F_Q is ~40 in our imaging system (see Figure 8). This F_Q value was used to convert the ΔF histogram to a Pr distribution of individual

synaptic terminals (Figure 1C). The Pr-distribution has a skewed shape favoring low values (median= 0.14). Application of 30 APs under such conditions would ensure the detection of functional terminals with Pr >0.04.

Since only those synaptic terminals with Pr > 0.04 were detected, we hypothesized that there must exist a population of terminals with lower Pr which were not being detected by this procedure. To determine both the number and the proportion of very low Pr terminals to total functional synaptic terminals, we compared the co-localization of FM puncta obtained from the 30 AP loading with puncta obtained using fluorescent antibodies against specific presynaptic proteins. VGLUT1 and GAD-65 antibodies were used to mark glutamatergic and GABAergic terminals, respectively. After FM images were obtained, the specimens were rapidly fixed and stained with antibodies (see Experimental procedures). The two sets of images were aligned, allowing comparisons of functional terminals with their structural equivalents (Figure 1E). Most FM puncta were co-localized with spots labeled by antibodies against presynaptic proteins (Ryan et al., 1993; Schikorski & Stevens, 2001). To ensure that these functional presynaptic boutons were part of functional synapses, composed of both pre- and post-synaptic machinery, we examined whether spots labeled by VGLUT1 antibody were co-localized with those marked by PSD-95 antibody, a critical protein present in the postsynaptic spine of glutamatergic synapses. All VGLUT1 spots were co-localized with PSD-95 spots (Figure 1G). Thus, the majority of FM dye uptake occurred specifically within structurally complete synaptic terminals. However, not all synaptic terminals took up FM dye after 30 APs (Figure 1E). In fact, only 46% of structural

synapses were stained during the 30 AP stimulation/loading protocol (Figures 1E and 1F). To determine the functional status of these seemingly non-functional terminals, we increased the technique's sensitivity by increasing the number of APs to 150 and the frequency of stimulation to 5 Hz. This protocol facilitates the release of vesicles from low Pr synapses without causing extensive depression of high Pr synapses (Murthy et al., 1997). Twenty percent more functional synapses were detected by this procedure, which is consistent with a previous report (Murthy et al., 1997). To determine whether the remaining 30% of synapses were capable of having vesicle turnover at all, we applied a maximal stimulation protocol (600 AP@ 20 Hz). Compared with labeling under the 30 AP protocol in the same region, the number of FM-positive puncta that correlated with structurally identified synapses doubled to 88%.

We have interpreted the lack of FM uptake after 30 action potentials as meaning that the terminals have too low a Pr to exocytose their vesicles even after such a sequence of depolarizing events. An alternative possibility is a potential failure of action potentials to reach synaptic terminals. We considered this unlikely for the following reasons: (i). Synaptic failure in hippocampal slices could not be attributed to the failure of action potential propagation to synaptic terminals at the low stimulation frequency (Allen & Stevens, 1994; Raastad & Shepher*d, 2003)*. (ii) It has been demonstrated previously that Ca^{2+} flux in synaptic terminals is reliably generated in cultured hippocampal preparation (Mackenzie, Umemiya, & Murphy, 1996; Ryan & Smith, 1995). (iii). The numbers of FM positive puncta detected after maximal electrical stimulation (600 AP @ 20 Hz) were similar to those obtained by 50 mM K^+ stimulation

(Figure 1F), a method that depolarizes all terminals directly by generating prolonged opening of Ca^{2+} channels (Betz, Mao, & Bewick, 1992; Ryan et al., 1993). (iv). In the presence of 100 ng/ml of neurotrophin BDNF, which is known to increase the Pr of synaptic terminals without changing their electrical excitability (Li, Zhang, Lester, Schuman, & Davidson, 1998), we found that all structural synaptic terminals became capable of taking up FM dye with the 30 AP protocol (see Figure 3B).

In summary, our results show that most synapses had a relatively low Pr (median=0.14), and that roughly fifty percent of all structural synapses had a Pr<0.04.

Synapses with low probability of release are not potentiated by theta burst stimulation

Given the inverse relationship between the initial strength and plasticity of a synapse (Bi & Poo, 1998), these low-Pr terminals should in theory be highly potentiable. To test this possibility, we employed a plasticity induction method that is believed to replicate neural activity *in vivo* – theta-burst stimulation (TBS) (Bliss & Collingridge, 1993). The induction-associated changes in Pr of synaptic terminals were determined by comparing ΔF_1 and ΔF_2, before and 30 minutes after TBS (30 bursts, each containing 5 APs @ 25 Hz, 500 ms inter-burst interval). Surprisingly, no potentiation of Pr, indexed through significant changes in FM dye loading, was observed following the theta-burst induction protocol (Figure 2A, a-c). No changes were found either in the distribution of release probabilities (Figure 2C) or in the slope of $\Delta F_2/\Delta F_1$ (Figure 2F, blue circles). On average, $\Delta F_2/\Delta F_1$ (ratio of fluorescence signal per FM spot) was 0.9±0.2 and N_2/N_1 (ratio of the number of detectable FM positive terminals) was 1.2±0.2 (Figure 1H). We also employed F×N to represent the total synaptic strength (S) within a given region of the hippocampal network. There were no significant differences in S_2/S_1 (1.1±0.4, n=8432, N=13, p=0.15). This lack of potentiation was also observed 10 minutes following induction protocol, also suggesting a lack of short-term potentiation (n=3671, N=5, p=0.3). To confirm that the applied induction protocol was sufficient to reach the LTP threshold (Bear, 2003), we quadrupled the total number of action potentials used for TBS induction (600 AP). Still, no detectable changes of synaptic strength were found

(S_2/S_1 = 1.2±0.4, n=3903, N=4). These data suggest that low Pr synaptic terminals are not by default potentiable with TBS, leading us to ask what conditions would make such synapses plastic.

Reduction of neuronal activity triggers enhancement of synaptic plasticity

Since the increase in neural activity during the maturation of neural circuitry is associated with a reduction in the plasticity of synapses, we hypothesized that the level of neural activity in networks might directly influence the plasticity of synapses. If so, a reduction of neural activity would help convert non-plastic synapses into plastic ones. To test this possibility, we pretreated culture neurons for 4 hours with 100 nM TTX, a concentration blocking 95% of neuronal activity (Fig. 4D). Using the induction protocol described above, we tested the plasticity of presynaptic terminals in the TTX-treated cultures (Figure 2B; the treatment drug was not present during induction protocol). In this case, there was an increase in FM dye loading after TBS and thus measured Pr of the synaptic terminals, although the initial Pr of synapses did not change significantly (Figure 2A, d-f). Quantitatively, there were two distinct changes in FM 1-43 staining properties after TBS-mediated induction: (i) an increase in the fluorescence intensity of puncta detected in the basal condition, indicating an increase in the average Pr; and (ii) an increase in the total number of detected FM-positive boutons, indicating a conversion of terminals with a Pr<0.04 (undetectable) to a state of Pr >0.04. Since this phenomenon was observable 10 minutes after TBS, we concluded that synaptogenesis was unlikely. For the experiment depicted in Figure 2A(d,e), the median value of ΔF_2 increased two-fold after the TBS protocol, while the number of detectable fluorescent spots increased from 508 to 1608 (Figure 2D). The collective results of these experiments (n=4328, N=7; where n is the number of terminals and N is the number of experiments) are shown in

Figure 2G. After TBS, the probability of release, on average, increased 1.8-fold ($p<0.001$), accompanied by a simultaneous 3-fold increase in FM-positive synaptic density ($p<0.001$). Total presynaptic strength (S) increased 5.4-fold after induction in the TTX-treated cultures (red bars). This potentiation was also long lasting: a stable increase in synaptic strength was detected from 10 minutes to 1.5 hours after TBS (Figure 2E). We refer to this pre-synaptic potentiation as plasticity throughout the rest of the paper. Thus, a reduction of AP generation through TTX-mediated blockade of Na^+ channels can induce an enhancement of synaptic plasticity.

Since it is known that the activation of NMDARs during TBS is essential for the induction of synaptic plasticity, we tested whether a TBS-induced increase of Pr requires NMDAR activation. No detectable changes in ΔF were observed if the NMDAR blocker AP-5 (50 μM) was present during theta-burst delivery ($n=4207$, $N=5$, $p=0.2$, Figure 2G, yellow bars), indicating the necessity of NMDARs for inducing this type of synaptic plasticity.

BDNF release is necessary for TBS-induced presynaptic potentiation

We further characterized the signal involved in relating TBS to presynaptic potentiation. Recent studies have indicated that the release of BDNF is required in the expression of the presynaptic component of theta burst-induced potentiation in hippocampal CA3-CA1 synapses (Kang, Welcher, Shelton, & Schuman, 1997; Zakharenko et al., 2003). We used an extracellular TrkB-IgG fusion protein that chelates endogenously-released TrkB ligands to block this putative pathway (Shelton et al., 1995). Application of TrkB-IgG (4 μg/ml) to hippocampal cultures 5 minutes prior to induction protocol (TBS) blocked TBS-induced presynaptic potentiation (S_2/S_1 = 5.1±0.5, n=3896, N=4 in control group; S_2/S_1 = 1.3±0.1, n=4407, N=5 with TrkB-IgG; Figure 3A). The presence of TrkB-IgG did not alter the properties of the presynaptic terminals under the basal condition or alter synaptic NMDA currents measured by double-patch recording (data not shown), confirming that endogenously released BDNF is necessary for the induction of presynaptic plasticity.

To confirm the role of BDNF in presynaptic potentiation, we studied the effects of exogenous application (3 minutes) of BDNF on the Pr of presynaptic terminals. Consistent with previous findings (Li et al., 1998), the Pr of presynaptic terminals can be upregulated directly by application of BDNF (EC50=25 ng/ml) (Figure 3B). Given the variety of cellular pathways that BDNF stimulates (B. Lu, 2003), we wished to use the lowest possible concentration to avoid the wide range of possible non-specific effects. For this purpose, we examined whether the presynaptic efficacy of BDNF would be

higher when the neuronal membrane is depolarized, as has been shown previously in the developing NMJ (Boulanger & Poo, 1999). We used TBS to depolarize while applying cadmium and AP-5 (both at 50 μM), blockers of VGCC and NMDA channels respectively, to prevent Ca^{2+} dependent release of endogenous BDNF. Under this condition (referred to as V+), there was no presynaptic potentiation (Figure 3B; left-most point). When BDNF application was coupled with depolarization (V+), BDNF's efficacy was enhanced ten-fold (EC50 = 2.4 ng/ml, Figure 3B).

To determine whether BDNF/V+ and TBS-induced potentiation share the same pathway we performed an occlusion experiment. Acute BDNF/V+ applied at a saturating concentration (20 ng/ml) occluded potentiation by TBS (Figure $3C_1$), and BDNF/V+ failed to induce further potentiation after TBS (Figure $3C_2$). Given the mutual occlusion, these data suggest that BDNF is an endogenous messenger for TBS-induced presynaptic potentiation.

Enhancement of synaptic plasticity is induced by reduction of Ca^{2+} flux

Given that the rate of neural firing is largely dependent on the concurrent balance of excitation and inhibition, shifting this balance may be a physiological way of altering the overall level of neuronal activity (Liu, 2004) (Figure 4A). If so, enhancement of inhibition or decrease of excitation should be as effective in enhancing synaptic plasticity as blocking TTX-sensitive Na^+ channels. Flunitrazepam was used to prolong $GABA_A$ receptor opening time and enhance the strength of GABAergic transmission (5 μM, 4-6 hours). AMPA receptor (AMPAR) antagonist NBQX was used to decrease the strength of glutamatergic transmission (1 μM, 4-6 hours). Both treatments enhanced the plasticity of synapses. The probability of release, the number of FM-positive puncta, and the total presynaptic strength all increased after induction ($\Delta F_2/\Delta F_1$ = 1.5±0.1, N_2/N_1 = 2.5±0.2; S_2/S_1 = 3.8; n=3107, N=4; Figure 4B) in flunitrazepam-treated cultures. Similar results were found for NBQX-treated cultures: $\Delta F_2/\Delta F_1$ = 1.4±0.1, N_2/N_1 = 2.1±0.1; S_2/S_1 = 3.0 (n = 2709, N=4). Thus one can infer that a general reduction in activity, brought about by any of these means, is sufficient to induce potentiability in presynaptic terminals.

What intracellular mechanisms translate neural activity into modifications of synaptic plasticity? One natural candidate is Ca^{2+} flux through both NMDARs and VGCCs. The opening of both channels correlates strongly with global activity. Thus, we tested whether a reduction in Ca^{2+} flux is sufficient to enhance the plasticity of presynaptic terminals. Ca^{2+} influx to postsynaptic neurons is largely controlled by the opening of

NMDARs during synaptic transmission or via the opening of L-type VGCC during action potentials. Thus, we tested the effects of chronic reduction of NMDAR activity or L-type VGCC opening on the plasticity of synaptic terminals. The block of NMDARs by 20 μM AP-5 (n=2803, N=2) or that of L-type VGCC by 10 μM nimodipine (n=3321, N=3) enhanced the plasticity of synaptic terminals (Figure 4C). Since these treatments, particularly nimodipine, did not affect the level of neural activity significantly (Figure 4D), we conclude the reduction in Ca^{2+} flux was sufficient in itself to induce an up-regulation of synaptic plasticity.

Since we found that a transient reduction of neuronal activity for 4-6 hours increases the plasticity of the network, we asked whether a long-lasting reduction of neuronal activity, over a period of days, would generate similar results. To answer this question, we compared the degrees of synaptic plasticity after 4 and 48 hours of drug treatment, respectively. Surprisingly, after 48 hours of incubation there was no significant TBS-induced potentiation whether the drug inhibited global activity (TTX, NBQX, flunitrazepam, Figure 4E) or decreased Ca^{2+} flux (AP-5, nimodipine, Figure 4F). In both cases, the neurons appeared healthy. One possibility is that due to homeostatic mechanisms (rev. Turrigiano & Nelson, 2004) chronic inactivation led to a saturating increase of presynaptic efficacy (Bacci et al., 2001; Murthy, Schikorski, Stevens, & Zhu, 2001; Thiagarajan, Piedras-Renteria, & Tsien, 2002) which in itself made them incapable of being further potentiated. Indeed, we found that Pr increased by 50% after 48 hours of activity blockade (Figure 4G). However, the TBS-induced potentiation in the short-term treated cultures was over 400% (Figure 4G). Despite the modest increase of Pr,

these synapses had ample dynamic range to be potentiated. We can infer that the lack of plasticity during long-term reduction of Ca^{2+} flux is likely to be caused by other mechanisms.

Temporal patterns of NMDA-mediated Ca^{2+} flux can be modified by $[Mg^{2+}]_o$

It is puzzling that enhancements of plasticity were observable only if global reductions of neural activity or Ca^{2+} flux were restricted in time. Long-term reduction of neural activity must induce other biological changes that reduce the potentiability of synapses. Chronic perturbations of neural activity and calcium flux may disrupt normal function, leading to unexpected side effects. How, then, could the system induce physiologically relevant long-term enhancements of network potentiability? Since neither reducing global activity (through TTX, NBQX, or flunitrazepam) or Ca^{2+} flux (through blockade of just VGCC channels or partial blockade of NMDA receptors) was effective in long term treatments (Figure 4), we wished to examine whether selective reduction of different aspects of the network's patterns of Ca^{2+} flux would be capable of generating long-term potentiability.

In functional neural networks, the synaptic inputs induced by physiological stimuli tend to be correlated, while inputs from spontaneous activity of neural connections are uncorrelated (J. E. Lisman, 1997) (Figure 4A). The spatial and temporal structures of synaptic inputs are decoded into Ca^{2+} fluxes in postsynaptic neurons through the opening of NMDARs. By disturbing Ca^{2+} flux associated with one type of input and not the other, one might test the effects of various aspects of the patterns of Ca^{2+} flux on the synapses' potentiability. In that respect, the voltage-dependent effects of Mg^{2+} on NMDA channels were ideal for testing our hypothesis (Mayer, Westbrook, &

Guthrie, 1984; Nowak, Bregestovski, Ascher, Herbet, & Prochiantz, 1984). Since the effects of Mg^{2+} block are strongest at resting potentials, the extracellular concentration of Mg^{2+} ($[Mg^{2+}]_o$) influences Ca^{2+} flux during uncorrelated synaptic inputs. By contrast, during depolarization, the magnesium block is removed completely. Thus, an elevation of $[Mg^{2+}]_o$, increases the blockade of NMDA channels during hyperpolarization, selectively reducing Ca^{2+} flux associated with uncorrelated activity while leaving depolarization-associated Ca^{2+} flux relatively unperturbed.

Although the biophysics of Mg^{2+} block have been studied extensively (Jahr & Stevens, 1990; Mayer et al., 1984; Nowak et al., 1984), we wished to determine precisely the behavior of the Mg^{2+} block at near-physiological concentrations. For example, while the original studies looked at a range from 0.5 to 10 mM of Mg^{2+}, this mineral is found in rodent CSF at a concentration of around 0.8 mM (Chutkow, 1974), and in humans, CSF $[Mg^{2+}]_o$ fluctuates between 1.0 and 1.2 mM (Kapaki, Segditsa, & Papageorgiou, 1989). We evoked NMDA currents by iontophoretic application of glutamate to a putative single bouton identified by FM 1-43 labeling and recorded under whole cell patch clamp in the presence of the AMPAR blocker, NBQX (10 μM). The glutamate delivered by this technique can be focal and rapid (Murnick, Dube, Krupa, & Liu, 2002), with evoked NMDA currents' time course roughly comparable to that of $EPSC_{NMDA}$ (Renger, Egles, & Liu, 2001). When $[Mg^{2+}]_o$ was raised from 0.8 to 1.2 mM, it caused a 50% reduction of $EPSC_{NMDA}$ amplitude at -50 mV, while the size of the outward $EPSC_{NMDA}$ at +40 mV remained relatively unchanged. Further increases in $[Mg^{2+}]_o$ beyond 1.2 mM had significantly less effect on current.

To quantify this effect, we converted our measured NMDA currents into conductance (g) (Figure 4C). The voltage-dependency of the Mg block did not vary significantly with increases in $[Mg^{2+}]_o$. However, apparent affinity, K_{Mg}, changed dramatically when $[Mg^{2+}]_o$ increased from 0.8 to 1.2 mM (Figure 5C and Table 1, see Experimental procedures). Thus, within the known physiological range of CSF $[Mg^{2+}]_o$, small variations in $[Mg^{2+}]_o$ have profound influences on the affinity of Mg^{2+} for NMDAR. This region of high magnesium sensitivity could be used to selectively change the NMDAR-mediated Ca^{2+} flux near resting membrane potentials. To illustrate this effect quantitatively, we plotted the ratio of NMDA current amplitudes as a function of membrane potential at 0.8 and 1.2 mM $[Mg^{2+}]_o$ (Figure 5D). An increase in $[Mg^{2+}]_o$ from 0.8 to 1.2 mM led to a ~ 60% reduction of NMDA current when the membrane potential was below -50 mV, but had no effect at depolarized potentials.

It is known that NMDA channels are highly Ca^{2+} permeable (P_{Ca}/P_{Na} ~10) (Jahr & Stevens, 1993; Mayer & Westbrook, 1987) and that Ca^{2+} influx through NMDARs accounts for most of synaptic spine Ca^{2+} (Kovalchuk, Eilers, Lisman, & Konnerth, 2000; Sabatini, Oertner, & Svoboda, 2002; Yuste & Denk, 1995). In particular, since an elegant recent study by Sabatini et al (2002) has shown that the time course of Ca^{2+} influx during NMDARs opening matches exactly with the temporal profile of Ca^{2+} lifespan in the spine, measured NMDAR currents can be used to predict the size of the Ca^{2+} flux. However, since our conclusions rest on the effects that perturbation of Ca^{2+} flux has on synaptic plasticity, we wished to directly confirm that changes of Mg^{2+} concentration cause a proportional change in NMDA-mediated $[Ca^{2+}]$ transients at single spines. Individual

spines were visualized by filling the cell with both a fluorescent Ca^{2+} indicator dye (Fluo-5F) and Ca^{2+}-insensitive Alexa 633 (Sabatini et al., 2002) (Fig. 5E). NMDARs at a single spine were activated by local iontophoresis of glutamate while the resulting $[Ca^{2+}]$ transients were being monitored (Fig. 5F). Consistent with the studies mentioned above, we observed that the amplitudes of synaptic NMDA currents and of $[Ca^{2+}]$ transients at the spine were linearly correlated (r^2=0.99, Fig. 5G). Finally, to test whether Ca^{2+} flux has a similar sensitivity to $[Mg^{2+}]_o$ as NMDA currents, we compared the $[Ca^{2+}]$ transients and the NMDA currents at the same spines before and after an acute increase of $[Mg^{2+}]_o$. The amplitude of Ca^{2+} signal ($\Delta F/F$) and the amplitude of $EPSC_{NMDA}$ were reduced by 57±5 and 54±7 %, respectively (N=3, p>0.3). Thus, the NMDA-mediated currents and Ca^{2+} flux are sensitive to physiological variations of $[Mg^{2+}]_o$.

As a control, we determined that raising $[Mg^{2+}]_o$ from 0.8 to 1.2 mM did not alter resting membrane potential (74±1 mV at 0.8 mM; 73±1 mV at 1.2 mM, N=5), nor overall synaptic inputs during network activity ($EPSC_{1.2}/EPSC_{0.8}$ = 1.03±0.1, N=5). Furthermore, there were no detectable changes in spontaneous miniature $EPSP_{AMPA}$s ($EPSP_{1.2}/EPSP_{0.8}$ = 0.9±0.1, N=5). The lack of detectable influence on the excitability of neurons and synaptic inputs during network activity can be explained by the relatively small increase in $[Mg^{2+}]_o$, which is insufficient to significantly alter the excitability of the membrane or the probability of transmitter release.

Elevation of $[Mg^{2+}]_o$ triggers formation of highly plastic synapses

We cultured hippocampal neurons with both "normal" and "elevated" concentrations of $[Mg^{2+}]_o$ (control: 0.8 mM - experimental: 1.2 mM; 2 weeks). Neurons growing under the higher level of $[Mg^{2+}]_o$ had normal neuronal density and morphology. Unlike the control neurons, however, their synapses were highly plastic even after long-term treatment. Figure 6A provides representative images of presynaptic terminals before and 30 minutes after TBS in high Mg^{2+} treated cultures. There are dramatic, sustained increases in FM 1-43 staining after TBS stimulation. The Pr increased 2.3-fold (±0.1, $p<0.001$), and the number of detectable FM puncta increased 2.1-fold (±0.1, $p<0.001$), resulting in a 5.5-fold increase in total presynaptic strength (n=10618, N=15, $p<0.0001$, Figure 6B). This potentiation was stable for at least 1.5 hours (data not shown). This form of plasticity required NMDAR activation (50 μM AP-5 blocked induction; $S_2/S_1 = 1.1 \pm 0.2$, n=3691, N=5). In contrast to uniform reductions of Ca^{2+} flux (Figure 4F), synapses retained their plasticity in elevated concentrations of Mg^{2+}.

We attributed this effect to the selective influence of Mg^{2+} on Ca^{2+} flux associated with uncorrelated activity. However, the lack of long-lasting enhancement of plasticity with AP5-mediated blocking of NMDA channels (Figure 4F) may be due to the *complete* blockade of NMDA-mediated Ca^{2+} flux by AP-5. To determine whether this is the case, we repeated the experiment with a concentration of AP-5 (5 μM; ~ IC_{50}) that matched the degree of Ca^{2+} flux reduction obtained via an increase in $[Mg^{2+}]_o$. The magnitude of presynaptic plasticity was tested in cultures following 4 hours, 48 hours, 2

weeks, and 3 weeks of incubation with either 5 μM AP-5, 20 μM AP-5 or 1.2 mM $[Mg^{2+}]_o$. The response to 4-hour reduction of Ca^{2+} flux was very similar across all treatments. The magnitude of enhancement depended only on the degree of blockade. Complete blockade of NMDA receptor or L-type Ca^{2+} channels induced a ~4 fold enhancement of synaptic plasticity (Figures 4F and 6C). Reduction of NMDARs activity by 50%, whether through application of 5 μM AP-5 or increase of $[Mg]_o$ (0.8 to 1.2 mM), resulted in a ~2 fold enhancement of synaptic plasticity (Figure 6C). On the other hand, for long term treatments, only the synapses grown under elevated $[Mg]_o$ retain persistent high plasticity. Thus, it was not the scale of the blockade that determined the duration of plasticity enhancement. Rather, it was the blockade's preferential reduction of Ca^{2+} influx during periods of uncorrelated activity that generated a long-term increase of plasticity.

To test if the Mg^{2+}-induced effect was reversible, the cultures were incubated for 2 days in 1.2 mM $[Mg^{2+}]_o$ and then switched back to control conditions (0.8 mM $[Mg^{2+}]_o$). Exposure to 1.2 mM $[Mg^{2+}]_o$ for 2 days induced a 3.9-fold increase in total presynaptic strength after induction ($n=2234, N=3, p<0.001$; Figure 6D). The terminals in higher Mg^{2+} lost their plasticity and returned to control conditions 48 hours after being switched back to 0.8 mM $[Mg^{2+}]_o$ (S_2/S_1 is 1.1±0.2, $n=2739, N=3, p>0.2$). These data suggest that perturbations in Ca^{2+} flux can reversibly regulate the plasticity of synaptic terminals.

To confirm that such a prominent TBS-induced increase in Pr does contribute to the enhancement of total synaptic strength, the magnitude of potentiation was tested electrophysiologically by sampling field EPSCs (fEPSCs) before and after TBS. The whole cell recording was obtained under perforated patch configuration to avoid wash-out of the intracellular components critical for synaptic plasticity. The membrane potential was clamped at –70 mV and EPSCs were evoked by field stimulation at a sampling frequency of 0.03 Hz. $[Mg^{2+}]_o$ during sampling was 4 mM to reduce background neural activity. The intensity of field stimulation was adjusted to produce a half maximal fEPSC amplitude. After 30 minutes of sampling were employed to determine the baseline level of synaptic strength, the bath solution was changed to 1.2 mM $[Mg^{2+}]_o$ and the recording configuration to current-clamp mode to allow for membrane voltage fluctuations. TBS was delivered at the same amplitude and temporal profiles as for the FM experiments. In control cultures (Figure 6E-F), as expected, fEPSC size did not change significantly after TBS (0.9-fold change, $p>0.2$). In contrast, in the Mg-treated cultures, TBS induced a 2.7-fold increase in fEPSC amplitude ($p<0.0001$, Figure 6E-F). The increase in fEPSC reached a maximum ~10 minutes after TBS and lasted at least 1.5 hours. On average, no significant change of synaptic strength was found in control cultures (1.0±0.1, N=4), while synaptic strength increased 2.7-fold (±0.6, N=5) after TBS induction in the elevated Mg^{2+} treatment cultures (Figure 6G).

Up-regulation of NR2B is an important contributor to the enhancement of synaptic plasticity

Our finding that synapses grown under elevated $[Mg^{2+}]_o$ conditions are plastic allows us to identify attributes that determine the plasticity of synapses. The decline of developmental neuronal plasticity mirrors the change of NMDAR subunit composition, particularly a decrease of NR2B-containing receptors (Carmignoto & Vicini, 1992; Sheng, Cummings, Roldan, Jan, & Jan, 1994). Sensory deprivation, on the other hand, both prolongs ocular dominance plasticity and delays the developmental down-regulation of NR2B NMDAR currents (Philpot, Sekhar, Shouval, & Bear, 2001). In reduced preparations, blockade of neural activity or NMDA currents results in enhanced synaptic localization of NMDARs (Liao, Zhang, O'Brien, Ehlers, & Huganir, 1999; Rao & Craig, 1997). These experimental data suggest that activity-dependent regulation of NMDARs is correlated with modifications in the plasticity of synapses.

Thus, we tested whether the enhancement of synaptic plasticity is associated with an up-regulation of NMDAR function. EPSCs were recorded under double-perforated patch configuration (50 μM picrotoxin to block $GABA_A$ channel opening). The membrane potential was held at -70 mV to detect the AMPA component of the evoked response ($EPSC_{-70}$) and at +40 mV for detecting AMPA + NMDA components ($EPSC_{+40}$). $EPSC_{NMDA}$ was then calculated by subtracting a scaled $EPSC_{AMPA}$ from the $EPSC_{+40}$. Figure 7A shows representative EPSCs from neurons cultured under various $[Mg]_o$ showing that the decay of $EPSC_{+40}$ from elevated Mg^{2+}-treated synapses was significantly slower.

Further analysis indicated that this is associated with the slower decay of $EPSC_{NMDA}$ (Figure 7B). To get the relative strength of $EPSC_{NMDA}$ over $EPSC_{AMPA}$, we calculated an N/A ratio (defined as G_{NMDA}/G_{AMPA}, G being the integrated conductance of each current). Figure 7C shows that the N/A ratio increased significantly in elevated Mg^{2+} treatment neurons ($p=0.02$, N=5 for each condition). From this ratio and the charge transfer of quantal AMPAR mediated transmission (266 ± 23 fC, N=6), we calculated the quantal charge transfer through NMDARs (Q_{NMDA}, integrated from t = 0 to 500 ms). Q_{NMDA} increased by 2.4 fold in neurons cultured with 1.2 mM $[Mg^{2+}]_o$ (Figure 7D). Given the 2-fold change in $EPSC_{NMDA}$ decay, this increase is likely to be entirely due to the prolongation of NMDA currents.

Previous studies have indicated that NMDA current duration is largely controlled by the subunit composition of NMDARs: receptors containing a larger proportion of NR2B subunits exhibit longer currents than those with a larger proportion of NR2A subunits (Flint, Maisch, Weishaupt, Kriegstein, & Monyer, 1997; Tovar, Sprouffske, & Westbrook, 2000; Vicini et al., 1998). The prolonged decay of $EPSC_{NMDA}$ in the elevated Mg^{2+}-treatment neurons might result from an increase in the number of NR2B-containing NMDARs. To test this possibility we determined the sensitivity of $EPSC_{NMDA}$ to ifenprodil, a selective NR2B blocker, in control versus experimental neurons. Figure 7E shows that, indeed, the ifenprodil-sensitivity of $EPSC_{NMDA}$ in elevated Mg-treated cultures is much higher than in the controls. On average, in 1.2 mM Mg-treated cultures, an application of 3 μM ifenprodil reduces the total charge transfer by 80% (±4, N=5,

$p<0.001$). In contrast, in control cultures, the total charge transfer was reduced by only 45% (±2, N=6, $p<0.01$, Figure 7F).

These results suggest that on the postsynaptic side, a reduction in background Ca^{2+} flux induces a 50% increase in NR2B-containing NMDARs and the N/A ratio. To directly evaluate the role of increased NMDAR function in the enhancement of plasticity of presynaptic terminals, we applied the NR2B-selective antagonist ifenprodil (1 μM, current reduced by 53% (N=3, $p<0.01$)) to *cancel* the up-regulation of NMDAR function induced by the elevation of $[Mg^{2+}]_o$. If the plasticity we observed was due to changes strictly other than increased NMDAR function, then this perturbation should have had no effect on the enhanced potentiation. However, the magnitude of potentiation was reduced by 50% suggesting an involvement of NMDARs up-regulation in the enhancement of synaptic plasticity (Fig. 7G). This data also suggests that other mechanisms are at play. Increased NMDARs function is likely to be an important but not sole factor in the enhancement of synaptic plasticity.

Discussion

Inverse relationship between the level of neural activity and plasticity of synapses

Changes in synaptic activity have been shown to lead to persistent changes in the direction or magnitude of synaptic plasticity, a phenomenon that has been called meta-plasticity (Abraham & Bear, 1996). Previous studies have shown that even brief periods of several minutes of prior activity can influence the induction threshold of LTP or LTD. In this study, we focused on the long-term relationship between the level of neural activity and the plasticity of synapses. We showed that a reduction in network activity levels resulted in an increase in synaptic plasticity (Figure 4B). While previous work in primary sensory cortices, where plasticity is time-delimited by critical periods, has suggested this direction (see Introduction), we have directly established this link for hippocampal neurons, which are known to remain plastic during adult life.

Physiologically, the inverse relationship between neural activity and the plasticity of synapses may be important in the following way: In early phases of the formation of neural circuitry, immature but plastic synapses make weak synaptic connections. Functional strengthening of connections through Hebb-type coincidence detection mechanisms then helps establish computationally meaningful neural connections, leading to elevated overall levels of neural activity within networks. This increase in neural activity may in turn trigger, through the above mechanism, a reduction in the network's plasticity, which helps "stabilize" those newly strengthened synaptic

connections. The reversible nature of this relationship may be essential for the reorganization of in-vivo neural circuits when functional inputs are lost. Supportive of this perspective is that deprivation-induced synaptic reorganization is a generic property of adult neocortex. Visual and somatosensory neurons that are silenced by inactivation of primary inputs can acquire new receptive fields (rev Gilbert, Sigman, & Crist, 2001). This inverse relationship might facilitate synaptic reorganization mediated through Hebbian-type mechanisms.

Bursting Ca^{2+}, background Ca^{2+}, and plasticity

Our data suggests that the plasticity of synaptic terminals is regulated by the quantity (amount) and quality (pattern) of Ca^{2+} flux detected at the postsynaptic spine. In this regard, the enhancement of plasticity, in all of our treatments, is associated with a reduction of Ca^{2+} flux. However, uniform reductions of Ca^{2+} flux failed to induce long-lasting enhancements of synaptic plasticity, suggesting a complex role for Ca^{2+} flux in the regulation of presynaptic plasticity. The effects of reduction of Ca^{2+} influx on synaptic plasticity can be grouped into two temporal categories:

1) The response to short-term reduction of Ca^{2+} (~ 4 hours) is very similar across all treatments. The magnitude of this enhancement of synaptic plasticity is proportional only to the degree of Ca^{2+} flux blockade - the greater the reduction of Ca^{2+} flux, the greater the enhancement. For example, complete blockade of NMDA receptors or L-type Ca^{2+} channels induced a ~4 fold enhancement of synaptic plasticity (Figures 4F and 6C). On the other hand, reduction of NMDA receptor activity by 50%, whether through application of 5 μM AP-5 or an increase of $[Mg]_o$ from 0.8 to 1.2 mM, resulted in a ~2 fold enhancement of synaptic plasticity (Figure 6C). These similarities suggest a shared mechanism.

2). However, the response to long-term reduction of Ca^{2+} flux varied by treatment. The enhancement of plasticity lasted only transiently (< 24 hours) for uniform reductions of Ca^{2+} flux (AP5, TTX, flunitrazepam, nimodipine, Figure 4). On the other hand, voltage-dependent reduction of NMDA currents through increased Mg^{2+}

block generated a permanent enhancement of synaptic plasticity (Figure 6). This phenomenon suggests that long-term, non-specific reduction in Ca^{2+} flux might also induce other changes in neural circuits that prevent synapses from staying in a highly potentiable state. One interesting possibility is that the most important difference lies between the levels of Ca^{2+} flux induced by correlated versus uncorrelated activity. For example, the spatially restricted high levels of Ca^{2+} flux associated with correlated activity can induce potentiation of synaptic connections, while diffuse low levels of Ca^{2+} flux are believed to trigger long term synaptic depression (J. Lisman, 1989). It is possible that neural circuitry also distinguishes between these two spatial-temporal patterns in determining long-term properties such as intrinsic synaptic plasticity. The pattern of Ca^{2+} flux in spines could be modified either a. presynaptically, by altering the frequency-response relationship of transmitter release, or b. postsynaptically, by perturbing receptors and channels (NMDARs and VGCCs) that translate activity into Ca^{2+} flux. We chose magnesium, the endogenous voltage-dependent pore blocker of NMDARs, to alter the pattern of Ca^{2+} flux. We found that with an increase of $[Mg^{2+}]_o$ within the physiological range (0.8 – 1.2 mM), the plasticity of synapses was enhanced permanently (> 2 weeks, Figure 6).

What synaptic changes induced by higher concentrations of $[Mg^{2+}]_o$ were responsible for the enhancement of the synapse's plasticity? The reduction of background Ca^{2+} influx led to an up-regulation of NMDARs function, particularly an increase in the proportion associated with NR2B subunits (Figure 7E). Half-maximal blockade of the NR2B-containing NMDA receptors which restored NMDA currents to

their control values led to an inhibition of 50% of TBS-induced plasticity (Figure 7G). This substantial decrease clearly indicates that up-regulation of NR2B-containing NMDARs is important in the enhancement of synaptic plasticity. As noted in the introduction, previous studies in visual and somatosensory cortices have strongly suggested that critical periods of ocular dominance plasticity are matched with changes in NMDAR subunit composition. Mice that were genetically engineered to overexpress NR2B also show increases in hippocampal LTP and learning and memory function (Tang et al., 1999). Due to the substantial increase in NMDA currents (> 2-fold) and the accessible nature of our preparation, we are able to directly demonstrate a causal relationship between these two hippocampal processes.

It is important to also note that the reduction of NMDA currents to control levels did *not* eliminate plasticity. This indicates that the up-regulation of NR2B containing NMDARs is not the only relevant regulation point responsible for the enhancement of synaptic plasticity. This finding resonates with recent work in early sensory cortices showing that NR2B subunits and NMDAR currents may play only a limited role in determining their critical periods (Fagiolini et al., 2003; H. C. Lu, Gonzalez, & Crair, 2001). In addition, we note that NMDA currents increased after short-term blockade of activity and remained elevated after long-term inactivation, even when potentiation was no longer observable (unpublished data). All this suggests that the functional plasticity of pre-synaptic terminals is determined by multiple factors – only one of which is post-synaptic NR2-B composition. In this regard, increases in the affinity of the post-synaptic calcium sensor, the amount of BDNF release during TBS (Figure 3), or the

sensitivity of presynaptic terminals to the BDNF released may represent other critical regulation points. The ability to turn its plasticity on and off (Figure 6D) and to study its pre- and post-synaptic function separately make our uniquely reduced preparation an inherently attractive option for delineating the roles of the physiological and molecular attributes that determine the plasticity of hippocampal synapses.

Extending the ramifications of this work, it is important to note that Mg^{2+} is also an endogenous trace metal. This raises several questions related to the importance of this mineral in pathological states and putative mechanisms of physiological regulation. Mg^{2+} concentration in healthy human cerebro-spinal fluid (CSF) is known to be 1-1.2 mM (Kapaki et al., 1989; Woodbury, Lyons, Carretta, Hahn, & Sullivan, 1968). Given that our study shows the sensitivity of synaptic plasticity to $[Mg^{2+}]_o$ precisely in this range, we may conclude that maintaining proper $[Mg^{2+}]_o$ in the CSF is essential for maintaining the plasticity of synapses in vivo. Since it is estimated that the majority of American adults consume less than the estimated average requirement of magnesium (InstituteofMedicine, 1997), it is possible that such a deficit may have detrimental effects on synaptic plasticity resulting in potential declines of memory function.

Experimental procedures

Cell cultures and treatments

Hippocampi were dissected from postnatal day 1 rat pups and cultured as previously described (Tang et al., 1999). The experiments were performed in mature (>DIV 15) (Renger et al., 2001) high density cultures (synaptic density > 1.5 synapses/μm^2 of dendritic surface area). We used a culture medium containing 0.8 mM Mg^{2+} (Gibco, 51200-038) for control cultures and added various amounts of $MgCl_2$ to raise the Mg^{2+} concentration. For short-term (4-6 hours) and long-term (48 hours) reduction of activity or Ca^{2+} influx, the following drugs were added to the culture medium: 10 μM nimodipine (Tocris), 5 μM flunitrazepam (Sigma), 1 μM NBQX (Sigma), 5 and 20 μM DL-AP5 (Tocris), or 100 nM TTX (Biotium). All experiments involving animals were approved by the Massachusetts Institute of Technology's Committee on Animal Care.

FM dye loading and unloading

Functional presynaptic boutons were stained with 10 μM FM 1-43 (synaptogreen, Biotium) by eliciting 30 APs at 0.5-1 Hz. This loading protocol was chosen to avoid short-term plasticity and "re-use" of vesicles through "kiss-run" mode of exocytosis (Aravanis, Pyle, & Tsien, 2003). The neurons were stimulated to fire action potentials by passing 1ms 50mA current through platinum electrodes placed at a distance of 7 mm from both sides of the chamber. To ensure reliable action potential initiation, the current amplitude was chosen to be 50% above the threshold for action potential generation, as confirmed by whole-cell patch clamp recording. To prevent recurrent activity, excitatory

postsynaptic responses were blocked completely by the addition of DL-AP5 (50 μM, Sigma) and NBQX (10 μM, Sigma) during FM loading and unloading procedures. FM dye was present when terminals were stimulated and 30 s after the stimulation (Ryan et al., 1993). For single action potential loading, the duration of dye exposure was reduced to 15 s to minimize nonspecific staining. Following this loading protocol, any external dye that had not been taken up into terminals was washed away in Ca^{2+}-free solution with the addition of quencher ADVASEP-7 (100 μM, Sigma) to speed up dye removal from external membranes (Kay et al., 1999; Zakharenko, Zablow, & Siegelbaum, 2001). Unloading was induced by 2 Hz stimulation for 4 minutes.

Imaging and analysis

Imaging was taken using an Olympus (FV300) confocal laser inverted microscope. The 488 nm line of the argon laser was used for excitation, and the emitted light was filtered using a 510 nm long pass filter and detected by photomultiplier. A 40×1.15 NA water-immersion objective was used for imaging. For experiments including one AP loading (Figure8), images were collected at a resolution of 1024×1024 with a pixel width of 0.11 μm. Confocal aperture was set to maximal. Each image was the average of four images separated by 0.8 μm steps in the z-direction. For all other experiments, a confocal aperture was partially open and image resolution was reduced to 0.138 μm/pixel. The gain of the photomultiplier was adjusted to maximize the signal/noise ratio without causing saturation by the strongest signals. The image after FM dye unloading was subtracted from the initial image; thus only those terminals containing activity-dependent releasable FM dye (~90% of total staining) were analyzed. FM positive

puncta were selected for further analysis using custom scripts written in ImagePro Plus (Media Cybernetics, Carlsbad, CA) and MATLAB (Mathworks, Natick, MA) programs based on following criteria: the fluorescence intensity (ΔF) was 3 standard deviations above the mean background and the diameter of spots was between 0.1-0.6 μm.

Retrospective Immunohistochemistry

Following functional FM 1-43 staining, neurons were fixed by flooding the perfusion chamber with a fixative FSB solution consisting of 4% paraformaldehyde and 4% sucrose in 1x PBS for 30 minutes and permeabilized with 0.5% Triton X-100. Primary antibodies against VGLUT1 (Chemicon International), and GAD-65 (Chemicon International) were applied for 8 hours, followed by rinses in PBS and staining with Alexa 488- and 633-conjugated secondary antibodies (1/400; Molecular Probes, Eugene, OR) at 22-24°C. All images were collected at 1024 x 1024 pixels with a 0.069 μm/pixel resolution. 11 images separated by 0.8 μm steps in the z-direction were compressed to generate the final image. Images of the fixed and immunolabeled tissue were aligned with corresponding FM images of the same region.

Electrophysiology

Dual whole cell perforated patch clamp recordings were made on two interconnected cultured hippocampal pyramidal neurons. Perforated patch pipettes were front-filled with a solution containing (in mM): CsOH, 127; D-gluconic acid, 127; CsCl, 4; HEPES, 10; NaCl, 8; EGTA, 0.4; pH was adjusted to 7.25 with CsOH, and then back-filled with the same solution containing 150-220 ng/ml amphotericin B (Sigma, St.

Louis, MO). Extracellular solution contained (in mM): NaCl, 145; KCl, 3; glucose, 15; HEPES, 10; $MgCl_2$, 0.8-1.2; $CaCl_2$, 1.2; 0.005 glycine (Sigma), 0.05 picrotoxin (Sigma); pH adjusted to 7.4 with NaOH. $MgCl_2$ concentration was matched to its concentration in culture medium. In experiments where effects of drugs on neuronal activity were quantified (Figure 4D), recordings were done in culture medium (with HEPES replacing bicarbonate/$C0_2$ to maintain pH). All experiments were performed at room temperature. For assaying synaptic connectivity, each neuron was stimulated by 1 ms step depolarization from –70 to +30 mV in voltage-clamp mode. Only neurons with monosynaptic connections were used. The access resistances of both pre- and postsynaptic neurons were monitored online and were typically 7-20 MΩ. Recordings with access resistance > 20 MΩ or that varied substantially were rejected from analysis.

For studying the voltage-dependence of NMDAR Mg^{2+} block (Figure 5), NMDA currents were evoked by local application of glutamate using the high-speed iontophoresis technique (Murnick et al., 2002). The current traces for each cell were normalized to their value at +40 mV membrane potential. The voltage dependency of NMDA currents was modeled using the Woodhull function (Woodhull, 1973). The NMDA channel conductance in the presence and absence of Mg^{2+} was related according to the relationship:

$$\frac{g}{g_{\max}} = \frac{1}{1 + \frac{\left[Mg^{++}\right]_o}{K_{Mg}} e^{\left(-\frac{z\delta EF}{RT}\right)}} \quad (1)$$

where K_{Mg} is the voltage-independent affinity of Mg^{2+} for the channel (0 mV membrane potential), □ is the electrical distance of the Mg^{2+} binding site in the membrane field, *E* is membrane potential, and *z* is the valence of the blocking ion. RT/F was 25.4 mV (21°C).

Calcium imaging

Olympus (FV300) confocal laser-scanning system was used to perform calcium and structural imaging. The single wavelength calcium indicator Fluo-5F (K_d~1.6 μM, Molecular Probes) was loaded into the neuron under a whole cell patch clamping configuration. The intracellular pipette solution contained, in mM: 130 $CsMeSO_3$, 10 HEPES, 10 Sodium phosphocreatine, 4 $MgCl_2$, 4 Na_2-ATP, 0.4 Na_2-GTP, 0.02 Alexa Fluor-633 (Molecular Probes); pH was adjusted to 7.25. The pipette resistance ranged from 2-3 MΩ□and calcium imaging was performed at room temperature. For most experiments, images were taken 30-40 minutes after establishing whole cell recording to allow equilibration of indicators in spines located 50-150 μm from the cell body (where the actual measurements were performed). NMDA receptors at single spines were activated by local application of glutamate using high-speed iontophoresis every 20 sec. Fluo-5F and Alexa Fluor-633 were excited with two different wavelengths, 488 and 633 nm, by argon and helium lasers respectively. Imaging with Alexa Fluor-633 fluorescence was used to visualize dendritic morphology. To avoid photodynamic damage of the cell, the laser intensity was set to 0.1% (of 5 and 25 mW, respectively). This allowed us to obtain stable Ca^{2+} images over at least one hour. To measure the temporal profile of [Ca^{2+}] changes at the spine head, we used line scanning mode (500 Hz, Figure 5E-F). Baseline fluorescence (F_0) was measured for 50 ms prior to the stimulus

and $\Delta F/F$ was calculated as $(\Delta F/F)_t = (F_t - F_0)/F_0$. We periodically monitored AP-evoked $[Ca^{2+}]$ transients as an index of dendritic viability. Data analysis was performed using ImagePro Plus (Media Cybernetics, Carlsbad, CA).

Determination of fluorescence of a single vesicle (F_Q).

We have followed previously developed approaches to determine the value of F_Q (Aravanis et al., 2003; Murthy & Stevens, 1998; Ryan, Reuter, & Smith, 1997). Essentially, it is assumed that the number of vesicles exocytosed following a single AP should be small, in the range of one or two vesicles. Therefore, $\Delta F_{\#AP=1}$ (where AP=1 symbolizes that a single action potential was employed) should quantify the distribution of FM dye for a small number of synaptic vesicles. Figure 8A displays the FM dye puncta following a single AP loading procedure. Comparing it with the FM dye image obtained after 30 AP loading procedure, we find that fewer synaptic terminals were stained with FM dye in the former case, and for those terminals that did take up FM dye, $\Delta F_{\#AP=1}$ was significantly smaller than $\Delta F_{\#AP=30}$. On average, there is a 5.7 (±1.3)-fold difference between ΔF of the same boutons loaded with 1 or 30 AP (Figure 8C), suggesting a correlation between ΔF and the number of action potentials applied. To determine the value of F_Q, we identified the locations of functional synapses by the 30 AP-loaded image, and using this, obtained and plotted the intensity distribution of $\Delta F_{\#AP=1}$ (Figure 8D, 841 boutons). The F_Q was calculated by fitting the intensity of ΔF after single AP loading with the sum of multiple Gaussians (Aravanis et al., 2003)

$$T(\Delta F) = \sum_{k=0}^{3} v_k e^{-\frac{(\Delta F - kF_Q)^2}{2(\sigma_0^2 + k\sigma_v^2)}} \qquad (1)$$

where T is the number of events at a given ΔF, v_k is the amplitude of the *k*th peak, σ_0^2 is the variance of measurement error, σ_v^2 is the variance in fluorescence of a single FM1-43 labeled vesicle and was set to be $0.2*F_Q$ (Schikorski & Stevens, 1997). Thus, histograms were fitted by Eqn 1 with free parameters F_Q and $v_{k(0\ to\ 3)}$.

The distribution of $\Delta F_{\#AP=1}$ has discrete peaks, reflecting the quantal nature of fluorescent membrane dye staining, while the variance in each peak was assumed to originate from the noise of measurement and natural variation in vesicle size (Aravanis et al., 2003; Murthy & Stevens, 1998; Ryan et al., 1997). The 0^{th} peak, centered at the origin of the plot, represents functional synapses that failed to take up FM 1-43, while the first peak corresponds to boutons loaded with a single vesicle. Because of the lower number of events in the second and third peaks, their peak locations could not be determined conclusively. We determined the F_Q by fitting the histogram to the sum of four Gaussian functions with equal peak spacing and found F_Q to be 39.8 fluorescence units in the experiment shown in Figure 8D (see Experimental procedures; the average F_Q value from 4 experiments was found to be 41.2±1). Several additional tests were performed to confirm that the value of F_Q determined by this approach was proportional to the amount of FM dye releasable from a single vesicle. We found that the F_Q value was sensitive to dye concentration: it increased by 1.4-fold when FM 1-43 concentration was increased from 10 to 15 μM (see also Murthy & Stevens, 1998).

Furthermore, F_Q remained similar in experiments where only miniature release was measured (data not shown) (Ryan et al., 1997). Determination of F_Q permits us to monitor terminals with extremely low Pr. For example, applying 30 APs under such conditions will ensure the detection of functional terminals with Pr >0.04. Although increasing the number of action potentials would increase the sensitivity of detection of low Pr synapses, it would limit the upper bound of the dynamic range for detecting an activity-induced up-regulation of Pr.

Statistical analysis

Error bars shown represent the standard error of the mean (SEM). Statistical significance was considered to be $p < 0.05$ and is indicated in the figures by an asterisk. For each experimental condition that contributed to the analysis, N represents the number of separate cultures used and n represents the total number of individual synapses. Means were compared with the *t*-test.

Post-synaptic NMDA-R Normalization:

Activity-Dependent, Spatial and Temporal Properties

Introduction

NMDA receptors (NMDA-R) are known to play a central role in higher cognitive function and neural computation. Their activation is essential for most forms of synaptic plasticity and their genetic up-regulation and ablation in animal models lead, respectively, to enhancement and deficits in learning and memory (Tang et al., 1999; Tsien, Huerta, & Tonegawa, 1996). In humans selective blockade of NMDA receptors leads to substantial severe impairment of learning abilities (Rowland et al., 2005). NMDA receptors are necessary for sustaining the persistent patterns of neural activity that are understood as the substrates of working-memory function (Jackson, Homayoun, & Moghaddam, 2004; Wang, 2001). Sensory cortices fail to re-organize their sensory maps when these receptors are inactivated (Cline, Debski, & Constantine-Paton, 1987). Yet, notwithstanding the importance of NMDA receptors, there is broad variation in their expression across development and brain structures (Goebel & Poosch, 1999; Wong et al., 2002). The ability of neurons to participate in a variety of NMDA-R dependent processes depends on the underlying expression of these receptors (Cline et al., 1987; Goebel & Poosch, 1999; Jackson et al., 2004; Tang et al., 1999; Tsien et al., 1996; Wang, 2001; Wong et al., 2002).

Within neural networks, the level of NMDA-R activation determines not just the quantity, or magnitude, but the quality, or direction and spatial distribution, of synaptic plasticity (Nishiyama, Hong, Mikoshiba, Poo, & Kato, 2000; Polsky, Mel, & Schiller, 2004). A partial reduction of NMDA-R function transforms homosynaptic potentiation into its diametric opposite - heterosynaptic depression (Nishiyama et al., 2000). In terms

of neural response properties, synaptic inputs sum non-linearly when NMDA receptors are present, and sum linearly in their absence (Polsky et al., 2004). Thus, the availability of NMDA-R mediated activation at an glutamatergic synapse will both quantitatively and qualititatively affect its and the neuron's response properties.

During the early development, NMDA-R expression varies substantially across brain areas (Goebel & Poosch, 1999). However, the exact cause of this developmental down-regulation is unknown. Although one cannot rule out the involvement genetic programming in this receptor down-regulation, work across several labs indicates that increased levels of neural activity are causally involved in NMDA-R downregulation (Carmignoto & Vicini, 1992; Franks & Isaacson, 2005; Heinrich, Singh, Nordeen, & Nordeen, 2003; Philpot, Weisberg et al., 2001). In sensory cortices, for instance, across multiple experimental setups, the blockade of sensory inputs prevents the down-regulation of slow NMDA-R currents (Carmignoto & Vicini, 1992; Franks & Isaacson, 2005; Heinrich et al., 2003; Philpot, Weisberg et al., 2001). (Carmignoto & Vicini, 1992; Franks & Isaacson, 2005; Heinrich et al., 2003; Philpot, Weisberg et al., 2001) The association of increased activity and reduced functional NMDA-R activation leads to two key questions.

Firstly, what is the biological significance of this relationship? Is the decrease of NMDA-R function just a generic biological property - similar to how increases of inhibition always lead to decreases of firing rates – or is there a finely tuned process of negative feedback that keeps NMDA receptor activation constant over time – perhaps similarly to how

firing rate homeostasis is believed to stabilize the activity of neurons (Turrigiano, Leslie, Desai, Rutherford, & Nelson, 1998).

Secondly, it is not known whether the NMDA receptor regulation couples all of a particular cell's synapses together or whether this happens sub-cellularly in a segmental fashion. Does the NMDA-R regulation happen only a whole neuron level in response to the total amount of synaptic inputs or can such regulation happen differentially at individual dendrites? The latter possibility would imply that individual dendritic compartments could independently control their plasticity and integrative properties (Cline et al., 1987; Jackson et al., 2004; Nishiyama et al., 2000; Polsky et al., 2004; Wang, 2001). The two alternatives paint remarkably different pictures of what is the minimal integrative unit of learning and computation.

In that last regard it should be stressed that while much is presently known on the ability of synapses to synergize locally by utilizing Hebbian processes, little is known on their ability to do the converse and regulate each other's intrinsic plasticity. When Hebbian plasticity is induced, we know that nearby synapses are potentiated, new spines are formed on contiguous dendritic branches, and local membrane excitability is enhanced (Engert & Bonhoeffer, 1997, 1999; Frick, Magee, & Johnston, 2004). These various 'localizing' processes suggest that a cluster of nearby and repeatedly coincident inputs would, through their cooperativity, develop 'hot spots' of synaptic strengths that could control the activity of the post-synaptic neuron(Goldberg, Holthoff, & Yuste, 2002). Yet, Hebbian processes work against the force of homeostatic mechanisms in setting synaptic strengths. To understand how synapses cooperate and compete in

influencing the post-synaptic neuron requires elucidating the spatial scale of both Hebbian and homeostatic processes. However, the spatial scale of no neural homeostatic process has been determined.

Given our interest in answering these two questions, a quantitative, reductionist approach is necessary. The decrease of NMDA receptor function with increased activity has been shown in a variety of systems (Carmignoto & Vicini, 1992; Philpot, Sekhar et al., 2001; Quinlan, Olstein, & Bear, 1999; Rao & Craig, 1997). While these have established the phenomenon, those conditions present challenges for biophysical studies of NMDA receptor regulation. Conceptually, the latter requires being able to generate and measure post-synaptic NMDA receptor responsiveness directly (i.e. without the effects of pre-synaptic terminals), repeatedly across long temporal periods (i.e. without damage induced by the technique itself), and focally if one is interested also in their spatial regulation. In the same way that the reductionist effort to study ionic channels produced now classic advances (Hodgkin & Huxley, 1952; Neher & Sakmann, 1976), a similar effort in quantifying activity-dependent receptor regulation is likely to produce useful insights (Hodgkin & Huxley, 1952; Neher & Sakmann, 1976). We have thus employed a technique of high-resolution iontophoresis and whole cell recording of hippocampal neurons to answer the above questions (Murnick et al., 2002). We show that NMDA receptor regulation quantitatively counters differences in synaptic input leading to a normalization of mean NMDA receptor activation. In a series of steps of increasing experimental control, we demonstrate NMDA receptor normalization counters differential synaptic input, artificial perturbations of NMDA-R

opening probability, as well as directly controlled NMDA receptor opening . Further, we show that activity-dependent NMDA receptor regulation can occur rapidly and focally – namely, in the time scale of 10s of minutes and at a sub-cellular spatial scale of 40-50 microns. These findings sketch a principle that must be incorporated in future frameworks that aim to understand neuronal computational processes.

RESULTS

Synaptic Input Determines Functional NMDA-R Density

Iontophoretic pipette delivery of a fixed amount of glutamate simultaneous with post-synaptic depolarization activates NMDA receptors (see Supplemental section). As previously shown, the spatial spread of high-resolution iontophoresis is local within 1-2 μms (Murnick et al., 2002) (compare with 10 ums in standard iontophoresis (Cash & Yuste, 1999)). We then dissociated the NMDA-R and AMPA-R mediated responses recorded somatically by averaging over a sufficiently delayed time-window (65-80 ms). In characterizing the stability of the responses, we find that repeated sampling of NMDA-R currents in the presence of intracellular BAPTA (5 mM) generates stable responses for at least 40 minutes (Figure 11B). In addition, we find that ~95% of the iontophoretically evoked NMDA-R response is mediated by the same population of synaptic receptors that are activated by pre-synaptic neurotransmitter release (also see Supplemental section) (Hardingham, Fukunaga, & Bading, 2002). The finding that this technique is focal, stable over long time periods, and samples synaptic NMDA-Rs make it then appropriate for the following studies.

Our interest centered on the functional density of NMDA receptors. This gives a measure of the NMDA-R activation per synapse. Due to the fixed spatial spread of glutamate release (Murnick et al., 2002), it can be inferred that the current recorded at the soma should be proportional to the number of functional receptors across the surface of an approximately cylindrical dendrite (Figure 9A) (Murnick et al., 2002). Thus the measured NMDA-R conductance (g_{NMDA}) in a given trial should scale linearly with

functional NMDA-R density and dendritic diameter. We find that when sampling various dendrites of a single neuron the peak NMDA-R conductance indeed co-varies linearly with visually-measured dendritic diameter (R^2=0.93, Figure 9B). To eliminate the effect of dendritic diameter on response size, we thus report the diameter-normalized functional NMDA-R density for our results.

As a first step, we wished to identify the quantitative relationship between synaptic input and NMDA-R regulation in individual neurons. We used perforated whole-cell patching to record from randomly selected pyramidal cells in hippocampal cultures. In such conditions, cells show spontaneous patterns of activity mediated through excitatory glutamatergic receptors (Liu, 2004). The average synaptic current input of each cell ($\overline{EPSC}$) was calculated by a simple mean over a time period of several minutes. As can be seen, different cells in a particular culture receive different levels of synaptic input (Figure 9C). The histogram of their average synaptic input demonstrates a wide non-normal distribution (Figure 9D). Because of this, we posited that the variation itself could be used as a tool to determine the relationship between activity and NMDA-R activation. Following initial sampling of mean synaptic input, TTX was washed in to block extraneous activity. Functional NMDA-R density was measured at multiple points over the dendritic tree of each cell. Plotting the average functional NMDA-R density against the cell's average synaptic input then reveals a distinct uni-modal distribution which can be described in two parts.

When the average synaptic input is sufficiently high, the functional NMDA-R density follows an inverse relationship to average synaptic input (Figure 9E). Interestingly, this

relationship is best fit by an inverse squared rather than inverse linear relationship (inverse linear-fit R^2= 0.74 vs. inverse square-fit R^2= 0.90; n=35 neurons). The fit is remarkably predictive as 90% of the functional NMDA-R density variance is explained by the average synaptic input of the cell. Yet, below a threshold of average synaptic input, functional NMDA-R density failed to be inversely correlated with activity.

The remarkable fit (R^2= 0.90) suggested to us that NMDA-R functional density is not just being reduced by greater synaptic input in a non-specific fashion. We posited that the NMDA-R regulation may be instead precisely compensating for changes in NMDA-R activation mediated by differential synaptic inputs. This would then lead to a conservation of average synaptic NMDA-R flux over time ($\int_0^t I_{NMDA} dt \Big/ t = k$). To examine the viability of the normalization hypothesis, we calculated mean synaptic activity multiplied by functional NMDA-R density and plotted it as a function of average synaptic input. Remarkably, we found that past a certain level of average synaptic input, the integral of NMDA-R flux over time is near-perfectly conserved (Figure 9E, inset). While this is a correlation and does not yet establish causality, it suggests that a process of quantitative normalization is involved in NMDA-R regulation.

Glycine Perturbation Causes NMDA-R Normalization

To test this we reasoned that a quantitative reduction NMDA-R activation should lead to a precisely compensating up-regulation of NMDA-Rs. Practically, we approached this question by perturbing the concentration of extracellular glycine. Glycine is an obligate co-agonist of NMDA-Rs(Forsythe, Westbrook, & Mayer, 1988; Sircar & Zukin, 1991). It is essential for activation of the receptor and its extracellular concentration determines in direct proportionality the NMDA-R currents generated by a given release of pre-synaptic glutamate (Forsythe et al., 1988; Sircar & Zukin, 1991). This effect is believed to be mediated through modulation of the channel's probability of opening (P_o)(Sircar & Zukin, 1991). We thus used controlled concentrations of glycine to quantitatively modify NMDA-R opening without drastic changing the gross activity of the circuit. Acutely reducing reduction of extracellular glycine from 1 uM to 50 nM in our preparation causes a ~2.5-fold decrease in NMDA-R responsiveness (ratio = 2.63 +/- 0.35; Figure 10A, left panel).

We thus chronically treated hippocampal cells in distinct glycine conditions (50 nM and 1 uM) for a period of 4-6 hours. By sampling functional NMDA-R density in a fixed extracellular concentration of glycine, we found that the functional NMDA-R density was relatively up-regulated in the 50 nM glycine case. Importantly, the degree of up-regulation was similar in magnitude to the acute effect of the perturbation itself (ratio = 2.29+/-0.10; Figure 10A, middle panel). When these neurons were tested in the same glycine concentration as that in which they were chronically treated, the functional NMDA-R density was statistically indistinguishable across groups (t-test p= 0.76; Figure

10A, right panel). Therefore, the amount of active NMDA receptors on the surface scaled properly to counter perturbations in the degree of NMDA-R activation. Mechanistically, the increase of NMDA-R responsiveness could be mediated through increased glycine sensitivity or a shift in voltage-dependency. However, the EC_{50} of the NMDA-R glycine site and the voltage-dependency curves were unchanged (Figure 10B and C). The normalization of NMDA-R responsiveness is likely mediated through changes in receptor number or sub-unit composition (Rao & Craig, 1997; Watt, van Rossum, MacLeod, Nelson, & Turrigiano, 2000).

Based on Figure 9E, we suspected that if the level of NMDA-R activation is below a certain threshold, NMDA-R normalization would no longer hold. To investigate whether this is the case, we generated a a series of permutations of the experiment shown in Figure 10A. Extra-cellullar [Ca]/[Mg] ratio is well-known to regulate pre-synaptic probability of release, and gross network activity in a circuit is modified in direct proportionality to it. To generate a condition of 'low activity,' we thus repeated the chronic treatment experiment under a substantially reduced extracellular [Ca]/[Mg] (~ 4-fold decrease from 1.2/0.8 to 0.6/1.6). In the context of 1 uM glycine, this caused an expected homeostatic increase of NMDA-R functional density (t-test $p < 0.05$; third bar from left, Figure 10D). Surprisingly, if glycine was further decreased to 50 nM, the absolutely functional NMDA-R density failed to move up, but moved down. When comparing the two glycine treatment conditions, in the context of this extreme [Ca]/[Mg] ratio, the functional NMDA-R density was now different between the two glycine treatment conditions (t-test $p < 0.001$; second pair of bars from left, Figure

10D). Thus, NMDA-R normalization was no longer applicable in the condition of substantially reduced [Ca]/[Mg]. Then, we repeated this experiment but combined it with an increase of neuronal plating density (50%). We find that in this last condition, the functional NMDA-R density became again indistinguishable between glycine treatment groups ($p=0.66$; Figure 10D, third pair of bars from left). The increase of neuronal density was able to counter the effects of extremely reduced [Ca/Mg] and return the cells to an NMDA-R normalizing state.

The non-normalizing state at very low activity levels may be the result of a pathologic process. However, no differences in structural morphology, neuronal density or electrophysiological properties could be discerned (data not shown). Importantly, it is noteworthy that the same phenomenon has been observed in-vivo. In the extreme condition where pre-synaptic release is entirely abolished in-vivo, whether in hippocampus or superior colliculus, this leads to down- rather than up-regulation of NMDA-R mediated currents (Colonnese, Zhao, & Constantine-Paton, 2005; Groc, Gustafsson, & Hanse, 2003). This may indeed represent a different regime of NMDA-R regulation to the normalization mechanism presented in this paper.

The above findings indicate that when the NMDA-R's probability of opening is experimentally modified, the biological regulation compensates for the perturbation. Consequently, mean NMDA-R current flux at synapses remains constant under these modified conditions.

Frequency of Coincident Events Determines NMDA-R Functional Density

In the next set of experiments, we wished to determine whether the NMDA-R normalization hypothesis holds when the probability of opening is instead made constant, but the frequency of channel opening is experimentally modified. Firstly, this would provide a further test of our hypothesis. Secondly, direct control of the channel's opening permits examination of the identity of the regulation signal. Conceptually, the signal that is normalized could be the maximal level of NMDA-R flux per individual event or the average NMDA-R flux over time. While glycine concentration modification causes changes in both, direct control of channel opening allows us to separate the two possibilities. Thirdly and finally, by directly controlling the level of NMDA-R activation at a local dendritic site, we can examine whether the ensuing normalization process takes place locally within dendritic compartments.

Our technique for measuring NMDA-R activation utilizes global depolarization and local application of glutamate molecules (see Supplementary section). Each such coincidence of glutamate and depolarization generates a measurable flux through local NMDA-R channels. Yet each such event should also regulate NMDA receptors in some spatial neighborhood of the application. We have thus conducted a series of experiments where we compared the effects of changing the frequency of sampling. This then acts as a controlled perturbations in the rate of channel opening events in the context of fixed probability of channel opening.

We combined perforated patch with trains of coincident events at frequencies of either once every ten or twenty seconds. Since the NMDA receptor regulation reported in this

paper is controlled by Ca++ flux (Fig. 3C), to focus especially on NMDA receptors self-regulation we blocked L-type VGCCs in the following set of experiments (nimodipine, 10 uM).

As previously shown, the initial functional NMDA-R density sampled in a randomly chosen cell varies broadly (Figure 9E). This variation appears to have originated from the stochastic intercellular variation in activity, and thus NMDA-R activation (Figure 9D and E). If so, when the frequency of NMDA-R activation is experimentally fixed to the same level in two separate cells with distinct prior activity histories, NMDA-R density should become similar. To test this possibility, we activated NMDA-Rs at a fixed frequency in distinct cells. Fig. 3A shows the change of functional NMDA-R density during this process. The initial functional NMDA-R density varied among sampled neurons. Strikingly, during the stimulation process, the NMDA-R functional densities across different cells converged toward the same values. Consequently, the local functional NMDA-R densities ended at nearly the same final value (Figure 11A). Statistically, this can be understood as a substantial decrease of functional NMDA-R density intra-group variance, namely a narrowing of the distribution (0.05 Hz caused a 89% *decrease* in G_{NMDA}'s variance when comparing initial and final distributions; Figure 11B). Note that each trace represents a separate experiment performed in a separate cell from a separate culture. Notwithstanding the variable initial conditions, they all approached a similar final G_{NMDA} value with a fixed rate of NMDA-R channel opening.

If it is true that the frequency of stimulation quantitatively controls the final NMDA-R value, a doubling of the first parameter should cause a halving of the second. To test

this, we repeated the above experiment in randomly chosen cells but now with a frequency of 0.1 Hz. We found that in this case as the above it led to a convergence towards a consistent final value (causing here a 75% *decrease* in respective G_{NMDA} variance; Figure 11B). As can be seen in Figure 11B, the distribution of NMDA-R densities after 20-40 minutes was statistically different depending on which stimulation frequency was used (0.05 Hz and 0.1 Hz led respectively to final mean G_{NMDA} values of 389 +/- 23 and 199 +/- 19 $pS / \mu m$; p=0.0001). Importantly, as predicted a doubling of the frequency of NMDA-R activation yielded a two-fold decrease in functional NMDA-R density (multiplying the lower functional NMDA-R densities by two made the two distributions statistically indistinguishable; t-test p = 0.84). This demonstrates that changes in the frequency of NMDA channel opening generate a normalizing change in NMDA-R expression. Furthermore, as shown in Fig. 3A, B, this could not be caused by a selection bias as the neurons for the two experiments were chosen in an inter-leaved and random fashion, and their initial NMDA-R density distributions were statistically indistinguishable from each other (p=0.69).

In relation to one of the questions formulated, it should be noted that while the channel opening frequency was different, the depolarization voltage and the glutamate release per event was identical across all experiments. Thus the maximal flux per NMDA-R opening event was the same. Yet, the two protocols led to different final functional NMDA-R densities. This pinpoints that it is the mean NMDA-R flux over time and not the maximal flux achieved at individual NMDA-R opening events that is the regulator of NMDA-R normalization.

Calcium is an important intracellular second-messenger and increases of intra-cellular Ca++ are a major effect of NMDA channel opening(Sabatini et al., 2002). We posited that intracellular calcium concentration may be the critical signal in regulating NMDA-R levels. To test this hypothesis, we repeated the above experiment in the presence of a fast-calcium chelator BAPTA (5 mM). Contrary to the results above, the mean and variance of initial and final values were comparable after 40 minutes of repeated sampling (initial G_{NMDA} = 408 +/- 190 $pS/\mu m$; final G_{NMDA} = 479 +/- 202 $pS/\mu m$; variance actually *increased* by 13%; 20 seconds/samples; Figure 11C). Thus, in the context of calcium chelation, functional NMDA-R functional density is constant and not affected by the frequency of channel opening (Figure 11B bottom). This also as mentioned previously demonstrates that our technique can generate stable, reproducible measurements over time.

NMDA-R Normalization is Spatially Local

The ability to directly control local glutamate release over long periods of time provides a foundation for studying the spatial dimensions of NMDA-R normalization at a sub-cellular level. The process could after all be taking place at the whole-cell level or independently within spatially confined dendritic compartments. This is relevant as the absolute level of NMDA receptor activation regulates the plasticity and integrating properties of individual synapses (Nishiyama et al., 2000; Polsky et al., 2004). Thus we were interested in knowing what is the minimal neuronal unit whose NMDA-R dependent meta-plasticity and integrating properties could be independently controlled.

To determine the spatial scale at which NMDA-R normalization operates, we started by measusing the local NMDA-R density at multiple neighboring sites on a dendrite of randomly chosen cells. We repeatedly activated NMDA-Rs by combining depolarization and glutamate release, and moving the iontophoretic electrode a fixed distance in between each recording. In the Figure 12A, the G_{NMDA} at each sampled location is shown and represented by the height of the black bar at that location. After the initial mapping of a portion of the dendrite, we placed the iontophoretic electrode at a position near the middle point of the mapped region. We then repeatedly activated NMDA-Rs at that location for a period of 20-40 minutes replicating the process shown in Figure 11. Finally, we re-obtained a map of local G_{NMDA} strengths just as we did at the beginning of the experiment (Figure 12A, red bars). As can be seen in this particular neuron, NMDA-R densities were altered significantly as a result of repeated, focal

NMDA-R activation. In brief, G_{NMDA} remained minimal at the location where NMDA receptors were repeatedly activated while they increased concentrically away from that position.

As expected, the initial distribution on the map appeared random which likely reflects the history of synaptic input across the dendrite. But after a period in which NMDA-R activation is controlled and thus non-random, this causes the final distribution to become non-random as well. This manifests itself in this case as a reverse Gaussian distribution.

One may expect that if we were to choose cells whose initial G_{NMDA} value were relatively high, stimulation should cause depression. The degree of depression will be a function of the stimulation frequency and, based on the single cell in Figure 12A, the distance from the point of glutamate delivery on the dendrite. We thus firstly selected cells whose average initial functional NMDA-R density was higher than the expected fixed end point of ~ 200 $pS / \mu m$ obtained for the 0.1 Hz stimulation trains (Figure 11). We then repeated the mapping process. When averaging across multiple neurons, it can be seen that the strongest decrease is found at the site of glutamate delivery while the locations most distal to it were least affected by the repeated NMDA-R activation (Gaussian distribution fit; 2σ = 44 microns; Figure 12B). This indicates that increased synaptic activity causes nearby synapses in particular to experience NMDA-R depression.

However, this leaves an open question: does that spatial range of action depend on the frequency of synaptic activation? rapidly activating glutamate release could, for

instance, modulate the whole neuron's inputs while a synapse that is less activate may be have spatially delimited effects.

For this last experiment, we repeated the experiment in Figure 12B, but using two frequencies of synaptic stimulation (0.05 and 0.1 Hz). To enable comparing broader spatial scales, we used a larger step size between G_{NMDA} measurements. We found firstly that as expected, for both frequencies the post-stimulation maps reveal a flaring pattern of increasing functional NMDA-R density with increasing distance (Figure 12C). Interestingly, the G_{NMDA} map obtained after activating NMDA-Rs at the slower frequency (0.05 Hz) appears visually to be a two-fold multiple of that obtained after the doubly faster stimulation (0.1 Hz). Indeed, when the maps obtained from either stimulation frequency are normalized by the NMDA-R density at the location of glutamate delivery, they overlap and are indistinguishable (Figure 12D). Thus, we find that for both stimulation frequencies the functional NMDA-R density doubles ($\lambda_{1/2}$) roughly every 40-50 microns (Figure 12D). This indicates that the spatial constant ($\lambda_{1/2}$) for NMDA-R normalization was the same irrespective of which frequency of NMDA-R activation was utilized. Synapses that are much larger than 40-50 microns away from each other were unlikely to affect each other's NMDA-R expression substantially. Given that in these experiments, as previously noted, extraneous activity was silenced by TTX, it is likely that the actual spatial scale of NMDA-R normalization is even smaller. It is however conceivable that a higher frequency of NMDA-R activation could lead to whole neuron NMDA receptor normalization.

Discussion

We have shown that post-synaptic functional NMDA-R density is regulated to quantitatively compensate for changes in its activation. This, by definition, generates a state of mean NMDA-R flux constancy (Figures 2 and 3). In a series of steps of increasing control, we have shown NMDA-R normalization precisely counters differential synaptic input levels across different cells, across artificial perturbations of channel opening probability, as well as in directly controlled local synaptic NMDA-R activation. We have referred to the process of mean NMDA-R flux conservation as NMDA-R normalization. This is to dissociate it from the oft-used terms of "NMDA-R homeostasis" and "dyshomeostasis" which have been repeatedly used in the literature to generically signify healthy versus pathological biological NMDA-R regulation (Hardingham & Bading, 2003). Normalization simply refers to the quantified counter-regulation of NMDA channels that leads to a conservation of mean NMDA-R flux.

What does NMDA-R normalization tell us more broadly about the dynamics of NMDA-R mediated flux and its associated calcium currents? We consider two cells that are otherwise identical except for having different levels of synaptic input. We then apply the well-known J-shaped $I_{NMDA}(V)$ current curve (Jahr & Stevens, 1990) andNMDA-R normalization as described in this paper .

In the low-activity cell, the averaged membrane voltage (V_m) fluctuates near the resting potential (–70mV). In the high-activity cell, due to constantly impinging synaptic inputs the average V_m is slightly depolarized near -60 mV. The latter would at first experience greater NMDA-R flux, because depolarization induces opening of the NMDA channel,

and reduction in the blockade mediated through Mg++ ions (Jahr & Stevens, 1990). This would then, based on our results, reduce the number and/or single-channel conduction of NMDA receptors so as to normalize total NMDA-R currents. As a result, the mean NMDA-R flux will be constant at some level we'll refer as k. Thus, if the NMDA-R number and single-channel conductance are properly modified to $N \cdot g_{NMDA} = k \cdot \mathrm{H}(\overline{V})^{-1}$, the average NMDA-R influx will be maintained constant across the cells, $\overline{I_{NMDA}}\big|_{low-activity} = \overline{I_{NMDA}}\big|_{high-activity}$ (see Appendix for details). Thus, notwithstanding a difference in the structural make-up of NMDA receptors, the total average current reaching the cells will be the same.

However, the arrival of a strong synaptic burst would expose the differences in NMDA-R expression between them. As noted above, one cell will have a larger reserve supply of NMDA-R receptors ($N \cdot g_{NMDA}$). Maximal depolarization would completely remove the Mg++ block and thus expose the entirety of the NMDA-R reserve. In this way, the otherwise hidden difference in NMDA-R expression across cells would become apparent. More specifically, in the low activity neuron, a synaptic burst would cause a 320% increase of NMDA-R flux as compared to mean levels (see Appendix for details). But in the high activity neuron, the same depolarization causes only a more modest 210% increase of NMDA-R flux. The synaptic burst in one case versus the other would be 50% larger in absolute terms ($H_{NMDA}(-60mV)/H_{NMDA}(-70mV)$). Similarly, the maximal Ca++ flux achievable with a burst in the low-activity cell will be ~70% larger than in its

counterpart. This calculation is conservative and the effect is likely to be larger in reality (see Appendix).

The synopsis of this analysis is that a weak level of synaptic input, through normalization, will lead to a higher level of "hidden" NMDA-R expression. This structural difference is likely to be then exposed by the arrival of a burst of synaptic input. It thus will endow the particular cell with a broader dynamic range in terms of both of maximally achievable NMDA-R mediated total current and Ca++ flux.

A broadening of the NMDA-R response dynamic range is relevant as NMDA receptors endow neurons with a wide variety of computational properties. For instance, their degree of activation determines whether inputs add supra-linearly, persistent patterns of activity can be sustained, and the direction, magnitude and polarity of synaptic plasticity achieved with synaptic bursts (Jackson et al., 2004; Nishiyama et al., 2000; Polsky et al., 2004; Wang, 2001). Putatively then a low-activity neuron endowed with more available NMDA receptors should behave qualitatively different from its high-activity counterpart. In relation the issue of supra-linear summation, recent computational work shows that its presence may determine whether neurons act as simple one-layer or more complex two-layer artificial neural networks (Poirazi, Brannon, & Mel, 2003). Thus, it stands to reason that a cell in the low-activity regime, and endowed with a large maximal NMDA-R flux, all else being equal, be more computationally complex and plastic than a high-activity cell.

Now consider that the two above hypothetical cells may represent two neurons in two different cortical structures. In visual cortex, for instance, the mean firing rate is known

to be relatively high, between 4 and 8.9 Hz, while in hippocampal circuits it is much lower and closer to 0.1-1 Hz (Baddeley et al., 1997; Legendy & Salcman, 1985). Speculatively, this suggests that the single neurons in these areas may have different computational properties due to their activity levels alone.

There are also indications that NMDA-R normalization may be a proxy of a more fundamental process of general intracellular Ca++ normalization. Firstly, we note that NMDA-R normalization is blocked in the presence of an intracellular fast calcium chelator, BAPTA (Figure 11C). Thus, NMDA-R normalization is likely Ca++ mediated. Secondly, it is well known that NMDA receptors account for the majority of synaptically induced Ca++ flux (Sabatini et al., 2002). Thirdly, we have also found that the activation of L-type VGCCs is as potent in regulating functional NMDA-R expression (data not shown). Fourthly, with aging, one observes an increase of L-type VGCCs that occurs simultaneous with a decrease in NMDA-R function (Toescu, Verkhratsky, & Landfield, 2004). It is thus conceivable that the connection is causal. Thus, this constellation of results suggests that NMDA-R normalization may be an electrophysiological representative of a more essential mechanism of Ca++ normalization. In that case, our conclusions regarding broadening of dynamic range in NMDA-R flux with low activity levels would suggest more generally a broadening of the Ca++ flux dynamic range. Given that Ca++ dynamics regulate a vast diversity of structural, functional and biochemical processes (Burgoyne, O'Callaghan, Hasdemir, Haynes, & Tepikin, 2004), a principle that determines its dynamic range is likely to be of importance.

More concretely, the above discussion provides an explanation for some our previous results (Slutsky, Sadeghpour, Li, & Liu, 2004a). In these, we used extracellular magnesium, the endogenous voltage-dependent blocker of these receptors, to chronically reduce average NMDA-R flux without disturbing maximal NMDA-R mediated flux. We subsequently found this leads to NMDA-R normalization near resting membrane potential. Yet, consistent with our present findings, with the burst of synaptic input associated with potentiation protocols the underlying NMDA-R up-regulation is exposed and results in increased plasticity in the high-Mg++ treated neurons.

In addition, we have found that NMDA-R regulation can take place rapidly, within tens of minutes. This rapid process could be mediated, as has been shown elsewhere, by a large mobile pool of NMDA receptors that are selectively captured by synapses dependent on their activity history (Groc et al., 2004). Thus coupling this technique with molecular imaging methods presents opportunities for directly controlling the movement of NMDA receptors and other activity-induced and dendritically targeted molecules. Similarly, we have demonstrated that that NMDA-R normalization is local. Due to the ability of this technique to generate repeated synaptic activation over long periods of time it could be also used to study the spatial scale of other forms of neural homeostasis - including AMPA receptors, spine numbers and dendritic channels (Turrigiano et al., 1998; Wallace & Bear, 2004).

Given that ours is the first measurement of the spatial scale of a homeostatic process, it carries a variety of predictions in relation to the spatial organization of synaptic inputs. Firstly, it is well known from theoretical studies that homeostastic mechanisms are necessary to prevent highly co-active neurons from over-taking the network's activity patterns. Thus AMPA homeostasis has been understood as stabilizing Hebbian plasticity (Turrigiano & Nelson, 2004). The presence of homeostatic mechanism at a local scale may achieve a similar end by preventing the firing of highly co-active synapses on individual dendrite from functionally over-taking the neuron. Because our measured scale of NMDA-R normalization closely matches that of the Hebbian processes by which synapses can cooperate it could counter their positive feedback (Engert & Bonhoeffer, 1997, 1999; Frick et al., 2004). Secondly, given the importance of NMDA receptors in functional and structural plasticity, this suggests that the carrying capacity, namely, the maximal total synaptic strength, and meta-plasticity of individual dendrites may be modulated independently. Thirdly, a local scale of NMDA-R normalization predicts that hippocampal dendrites that receive a high-level of synaptic input will integrate their inputs only linearly whereas that reveive lower levels may do so non-linearly (Polsky et al., 2004). Thus, this suggests that the integration properties, and thus computational power, of individual dendrites will depend on their specific levels of synaptic input (Poirazi et al., 2003).

Methods

Hippocampal cell culture and patch clamp recording

Primary cultures of CA1-enriched hippocampal neurons were prepared from neonatal rats (P1) as previously described(Tang et al., 1999). The age of the cultures used in this study ranged from 14 to 20 days in vitro (DIV). Whole-cell patch recordings were carried out as described elsewhere(Tang et al., 1999). For Figures 1 and 2, the composition of the recording electrode solution was (in mM): $CsMeSO_3$ 120, HEPES 10, NaCl 5, $CaCl_2$ 0.4, MgATP 2, NaGTP 0.3, and BAPTA 10, and was adjusted to pH 7.25 with CsOH. For the data in Figures 3 and 4, the perforated recording electrode solution was, in mM: CsOh 125, D-gluconic acid 125, CsCl 5, HEPES 10, NaCl 8, $MgCl_2$ 1, and EGTA 0.2. The amphotericin solution was freshly prepared at 150 ng/ml with the above intracellular solution. The unchanged solution was used to front-fill the pipette prior to back-filling with the amphotericin-loaded solution as described previously. The composition of the extracellular solution was always (in mM): NaCl 128, KCl 5, $CaCl_2$ 2, $MgCl_2$ 1, glucose 30, glycine 0.005, and HEPES 25 (adjusted to pH 7.4 with NaOH). Tetrodotoxin (TTX, 0.5 μM; Oretek Inc., Lake Oswego, OR) was added prior to recording to block action potentials in Figures 2, 3 and 4. For the protocol to determine synaptic versus extra-synaptic NMDA receptor composition, biccucculine (50 μM) and MK-801 (10 μM) (50 μM, Sigma, St Louis, MO) were added to the extra-cellular solution during the blocking period as indicated in the paper. For all experiments in this paper, only cells morphologically identified as excitatory Ca1-neurons were utilized.

The composition of the FM1-43 (Molecular Probes, Eugene, OR) staining solution for the image show in Figure 9 was (in mM): KCl 90, NaCl 39, Glucose 30, HEPES 25, $CaCl_2$ 2, $MgCl_2$ 1, NBQX (6-nitro-7-sulphamoylbenzo[f]quinoxaline-2,3-dione) 0.005, AP-5 (DL-2-amino-5-phosphonovalerate) 0.1, and FM 1-43 0.01 (adjusted to pH 7.4 with NaOH). Recordings were made with a 200B integrating patch clamp amplifier (Axon Instruments, Foster City, CA) with a 1 kHz (8-pole Bessel) low-pass filter. Data were digitized at 10 kHz using a Digidata 1200B A/D converter (Axon Instruments). Access resistance was monitored online and was typically <10 MΩ. AP-5 and NBQX were purchased from Tocris Cookson (Ballwin, MO). Following a 1 min incubation in the FM1-43 solution and a >5 min wash, neurons were visualized under a confocal microscope (Olympus Fluoview) using a 40x planachromat water immersion objective (1.15 NA).

Iontophoresis system

We used an MVCS 02 (NPI Electronic, Tamm, Germany) high-speed iontophoresis system to control transmitter release through the iontophoresis electrode as previously described (Murnick et al., 2002). We fabricated iontophoresis microelectrodes from quartz glass capillary tubes (O.D.=1.0 mm, I.D.=0.7 mm, Sutter Instrument Co.) pulled in a single stage with a horizontal pipette puller (Sutter Instrument Co. P-2000). These electrodes have a tip opening of approximately 0.1 μm, based on electron microscopy performed by the puller manufacturer. When filled with 150 mM glutamatic acid (pH adjusted to 7.0 with NaOH), they had a resistance of approximately 100 MΩ.

Occasionally, glutamate leaked slightly from the electrode tips, as visualized by increased noise in a patch recording when placed near a synapse. However, these leaks could be eliminated with 1–2 nA of positive holding current. Electrodes with a resistance of less than 80 MΩ tended to have larger leaks that were not controllable with holding current. We placed the electrode tip within 1.0 μm such that further lowering would not increase the recorded NMDA-R currents.

To properly adjust the capacitance compensation, we applied a −10 nA square-wave pulse at 20 Hz to the iontophoresis electrode after filling it and immersing the tip in the bath. We monitored the tip voltage on an oscilloscope while adjusting the compensation so that the voltage also described a square wave. This method also gave us a measure of the electrode resistance via the relationship $V=IR$. Typically the initial electrode resistance was >500 MΩ, possibly due to microscopic air bubbles in the tip. At this point, we 'zapped' the electrode once or twice with a −250 nA pulse for 5–10 s, after which the resistance would have a stable value around 100 MΩ. We reapplied a square wave periodically during the course of a recording session to monitor R and adjusted the compensation if necessary, but it typically varied very little over the course of several hours.

Glutamatergic Receptor Activation and Mapping

After iontophoretic electrode positioning, a brief square-shaped iontophoretic glutamate pulse (0.5 ms, -64 nA) was applied synchronous with voltage-clamp

depolarization (+40 mV; 500 ms depolarization ramp and by 900 ms of steady depolarization). This generated an outward current response (see Figure 13A).

The baseline was substracted using a line least-squares fit prior to glutamate release and ending near 900 ms after it. Using a window-averaging method (65 ms after glutamate release, width = 15 ms), we isolated the NMDA-R mediated component of the response. The iontophoretic electrode was lowered until the NMDA-R mediated response would not further increase. For Figures 1 and 2, where the intra-cellular contained the fast calcium chelator BAPTA (5 mM), this sequence was repeated and averaged across four times so as to minimize the noisy of effects of the high single-channel NMDA-R conductance. For this purpose as well, for Figure 11, the data points shown are a simple moving mean of the functional NMDA-R density over the last two minutes. This does not affect our conclusions as they do not apply to any time constants shorter than this interval.

For Figure 12, given that perforated patching was utilized, each spatial position shown was sampled only one or two times so as to minimize the effect that such mapping would have on NMDA-R regulation. During the intervening modification protocol, as described in the text, only one position received repeated bouts of glutamate release synchronous with depolarization to +40 mV. Thus, if the dendritic mapping at the beginning caused a slight modification this was constant across all conditions and dendritic locations. In addition, while the dendritic mapping lasted 2-4 minutes, the intervening modification protocol lasted roughly ten times longer, between 20 to 40 minutes. This ensured that the mapping procedure itself, and a putative regulatory

effect, could not affect the conclusions of our study. All mapping experiments were performed on the basal dendritic tree.

Ideally, our technique of long-term stimulation would have possessed a single-spine spread. Fortuitously given that the biological process of NMDA-R regulation as shown in the Results section appears to have a spatial scale of 40-50 microns, the resolution of 1-2 microns of the iontophoretic technique (Murnick et al., 2002), being at least an order of magniture smaller, is sufficient. We cannot however ascertain that it does not also operate at a single synapse resolution as well.

Modulation of the Dynamic Range of NMDA-R mediated Flux With Changes in Mean NMDA-R Activation

We will explore the difference in NMDA-R flux dynamic range between two hypothetical cells that have different levels of NMDA-R activation. In one, the average membrane potential is -70 mV ("low-activity cell") and while in the other it is -60 mV ("high-activity cell"). We then examine a conservation equation. This states that given some underlying average membrane potential $\overline{V}$, the number of receptors N and single channel conductance g_{NMDA} will be modulated such that the average NMDA-R current remains at some constant level k:

$$\overline{I_{NMDA}} = I_{NMDA}(\overline{V}) = N \cdot g_{NMDA} \cdot \mathrm{H}(\overline{V}) = k$$

Where $\mathrm{H}(V)$ describes the NMDA channel voltage-dependence (Jahr & Stevens, 1990). Thus, causing G_{NMDA}, the multiplier of N and g_{NMDA}, to be:

$$G_{NMDA}\big|_{\text{Given Some } \overline{V}} = N \cdot g_{NMDA}\big|_{\text{Given Some } \overline{V}} = k \cdot \mathrm{H}(\overline{V})^{-1}$$

We can then ask, given such conditions, what happens when a synaptic burst arrives that depolarizes both cells to -30 mV, namely, the voltage of maximal inward NMDA-R flux (Jahr & Stevens, 1990). We find that such a burst causing an increase of 320 and 210% when compared with the background level of influx, in the low- and high-activity cells respectively. Thus even though both cells receive the same level of average NMDA-

R influx, the low-activity cell generates a 50% larger NMDA-R influx with bursts of activity:

$$V_r = 0$$

$$\frac{I_{NMDA}(-30mV)}{I_{NMDA}(-70mV)}\Big|_{\bar{V}=-70mV} = \mathrm{H}(-30mV)/\mathrm{H}(-70mV) = 3.2$$

$$\frac{I_{NMDA}(-30mV)}{I_{NMDA}(-60mV)}\Big|_{\bar{V}=-60mV} = \mathrm{H}(-30mV)/\mathrm{H}(-60mV) = 2.1$$

$$\frac{I_{NMDA}(-30mV)|_{\bar{V}=-70mV}}{I_{NMDA}(-30mV)|_{\bar{V}=-60mV}} = \mathrm{H}(-60mV)/\mathrm{H}(-70mV) = 1.5$$

In other words, the low-activity cell has a broader NMDA-R mediated dynamic range. The difference is even more pronounced if one looks not not total current influx , but Ca++ flux. This is suggested to be the appropriate analysis given the findings shown in Figure 11C. Here we find that in that case there will be instead a larger - 1.7-fold difference - in the maximal NMDA-R mediated Ca++ flux when comparing the low- and high-activity cell:

$$V_r = 130$$

$$\frac{I_{NMDA}(-30mV)}{I_{NMDA}(-70mV)}\Big|_{\bar{V}=-70mV} = \mathrm{H}(-30mV)/\mathrm{H}(-70mV) = 6.0$$

$$\frac{I_{NMDA}(-30mV)}{I_{NMDA}(-60mV)}\Big|_{\bar{V}=-60mV} = \mathrm{H}(-30mV)/\mathrm{H}(-60mV) = 3.5$$

$$\frac{I_{NMDA}(-30mV)|_{\bar{V}=-70mV}}{I_{NMDA}(-30mV)|_{\bar{V}=-60mV}} = \mathrm{H}(-60mV)/\mathrm{H}(-70mV) = 1.7$$

Two points regarding these calculations' generalizability must be made. Here we have examined the normalization of NMDA-R currents when given different mean membrane potentials. Yet, it is obvious that this conclusion will apply equally well with any other

mechanisms that lead to changes in rates of NMDA-R activation: whether this be through changes in burst frequency or the timing between pre- and post-synaptic spikes (Jahr & Stevens, 1990; Koester & Sakmann, 1998). The demonstration is trivial.

For purposes of simplicity, we have assumed that both cells are being activated by the identical levels of glutamate release yet happen to somehow be depolarized at different degrees. In reality, the high-activity cell will also be exposed to a greater degree of pre-synaptic glutamate release. Thus, our calculation is a conservative estimate. This means that the modulation of NMDA-R dynamic range in more general conditions will be even more pronounced.

Statistical Methods

All error bars represent the standard error of the mean.

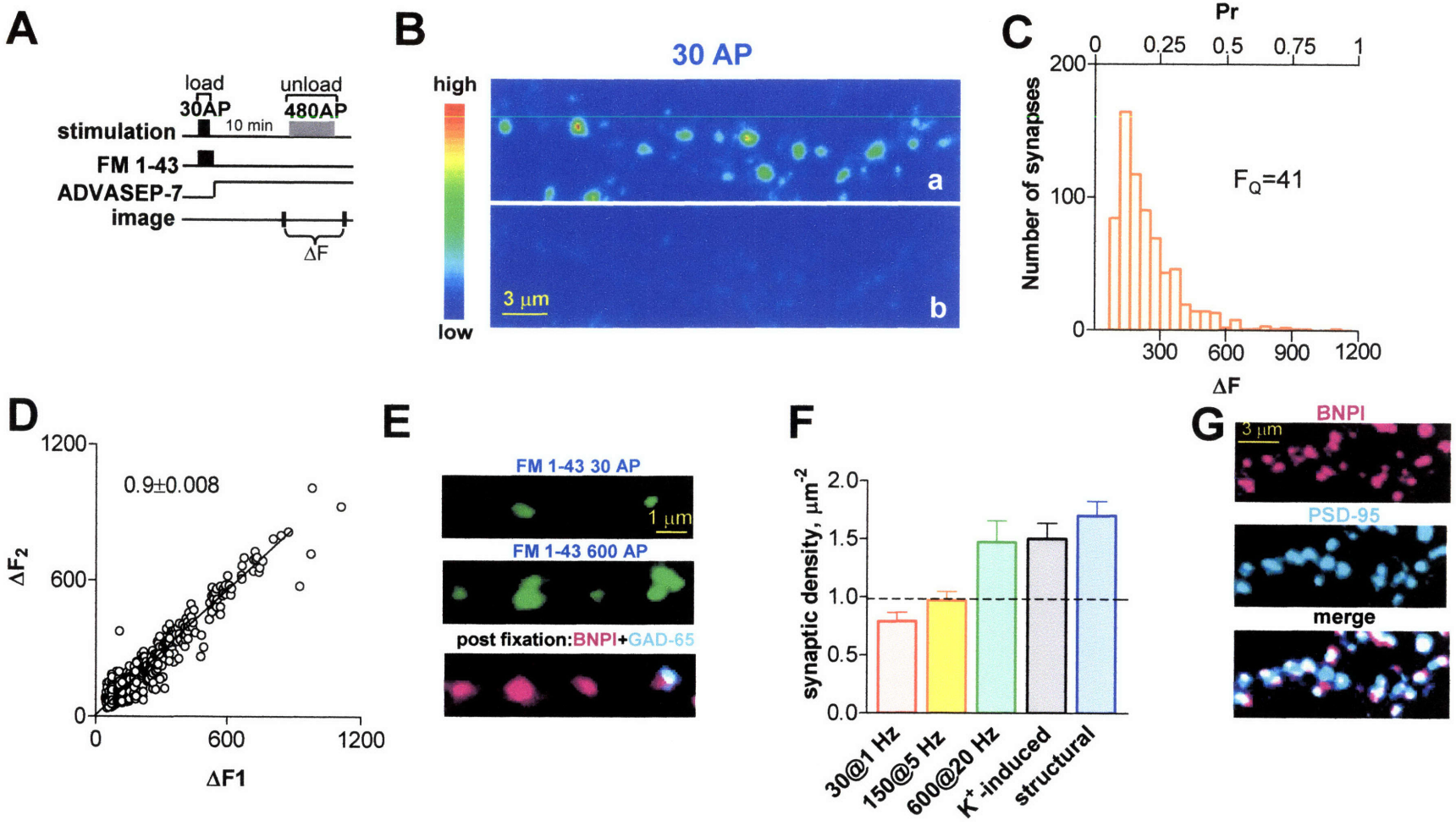
A
load
30AP
unload
480AP
stimulation
10 min
FM 1-43
ADVASEP-7
image
ΔF
B
30 AP
high
low
3 μm
a
b
C
Pr
0
0.25
0.5
0.75
1
200
100
0
Number of synapses
F_Q=41
300
600
900
1200
ΔF
D
1200
600
0
0.9±0.008
ΔF_2
0
600
1200
ΔF1
E
FM 1-43 30 AP
1 μm
FM 1-43 600 AP
post fixation:BNPI+GAD-65
F
synaptic density, μm^{-2}
2.0
1.5
1.0
0.5
0.0
30@1 Hz
150@5 Hz
600@20 Hz
K^+-induced
structural
G
BNPI
3 μm
PSD-95
merge

Figure 1

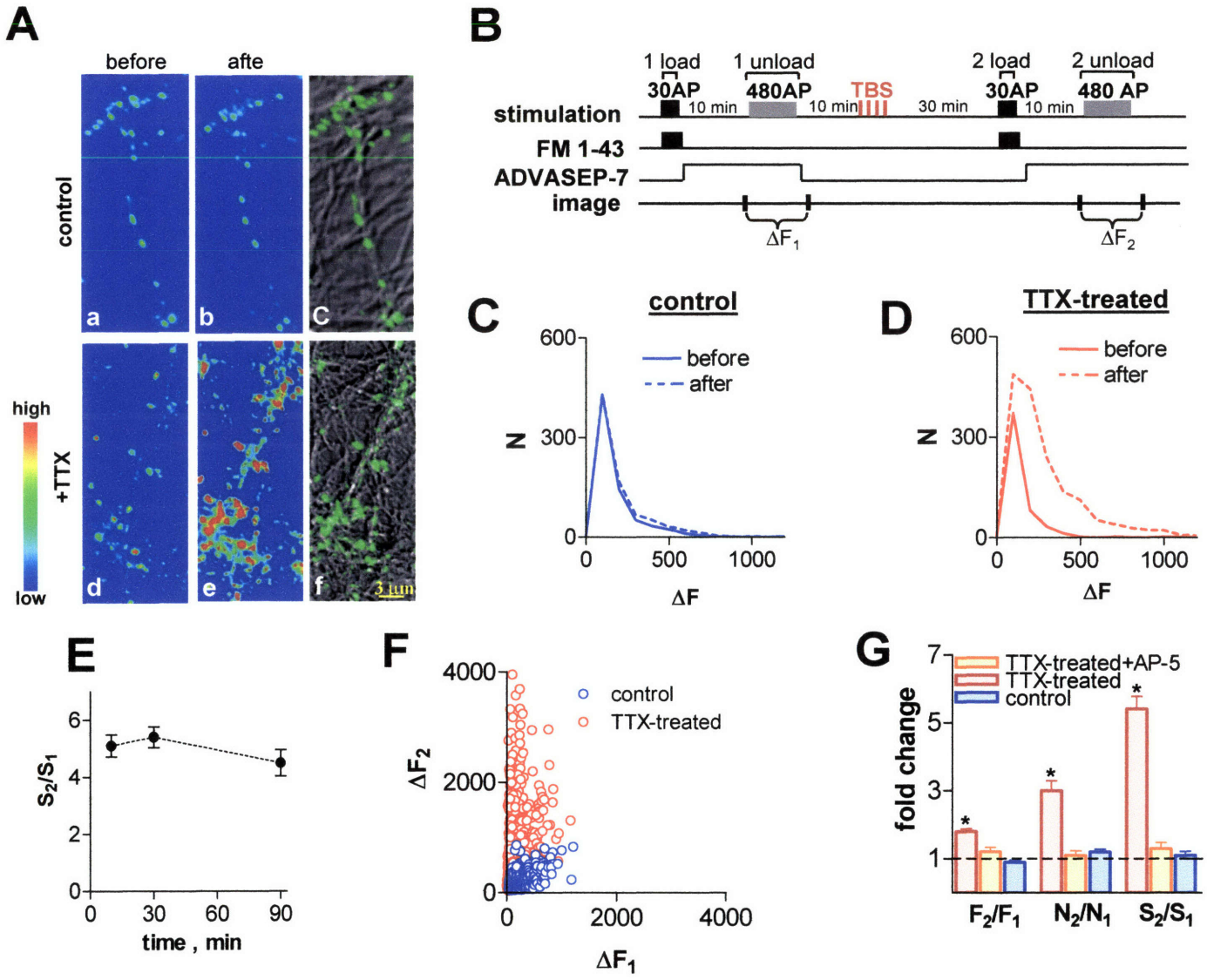
A
before
afte
control
+TTX
high
low
a
b
c
d
e
f
3 μm
B
1 load
1 unload
2 load
2 unload
30AP
480AP
TBS
30AP
480 AP
10 min
10 min
30 min
10 min
stimulation
FM 1-43
ADVASEP-7
image
ΔF1
ΔF2
C
control
before
after
N
600
300
0
0
500
1000
ΔF
D
TTX-treated
before
after
N
600
300
0
0
500
1000
ΔF
E
S2/S1
6
4
2
0
0
30
60
90
time , min
F
4000
2000
0
control
TTX-treated
ΔF2
0
2000
4000
ΔF1
G
TTX-treated+AP-5
TTX-treated
control
fold change
7
5
3
1
*
*
*
F2/F1
N2/N1
S2/S1

Figure 2

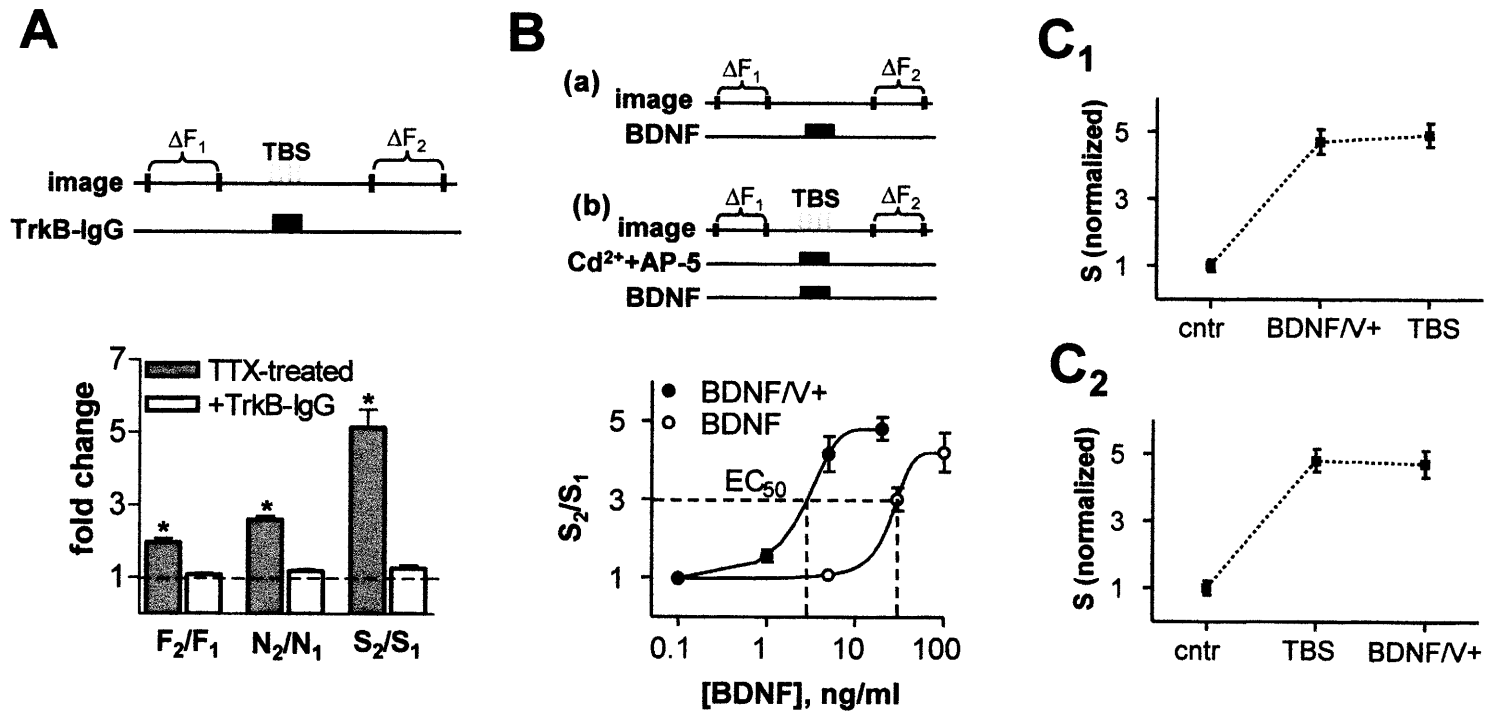
A
ΔF1
TBS
ΔF2
image
TrkB-IgG
TTX-treated
+TrkB-IgG
fold change
F2/F1
N2/N1
S2/S1
B
(a)
image
BDNF
(b)
Cd2+ +AP-5
BDNF/V+
BDNF
EC50
S2/S1
[BDNF], ng/ml
C1
S (normalized)
cntr
BDNF/V+
TBS
C2
S (normalized)
cntr
TBS
BDNF/V+

Figure 3

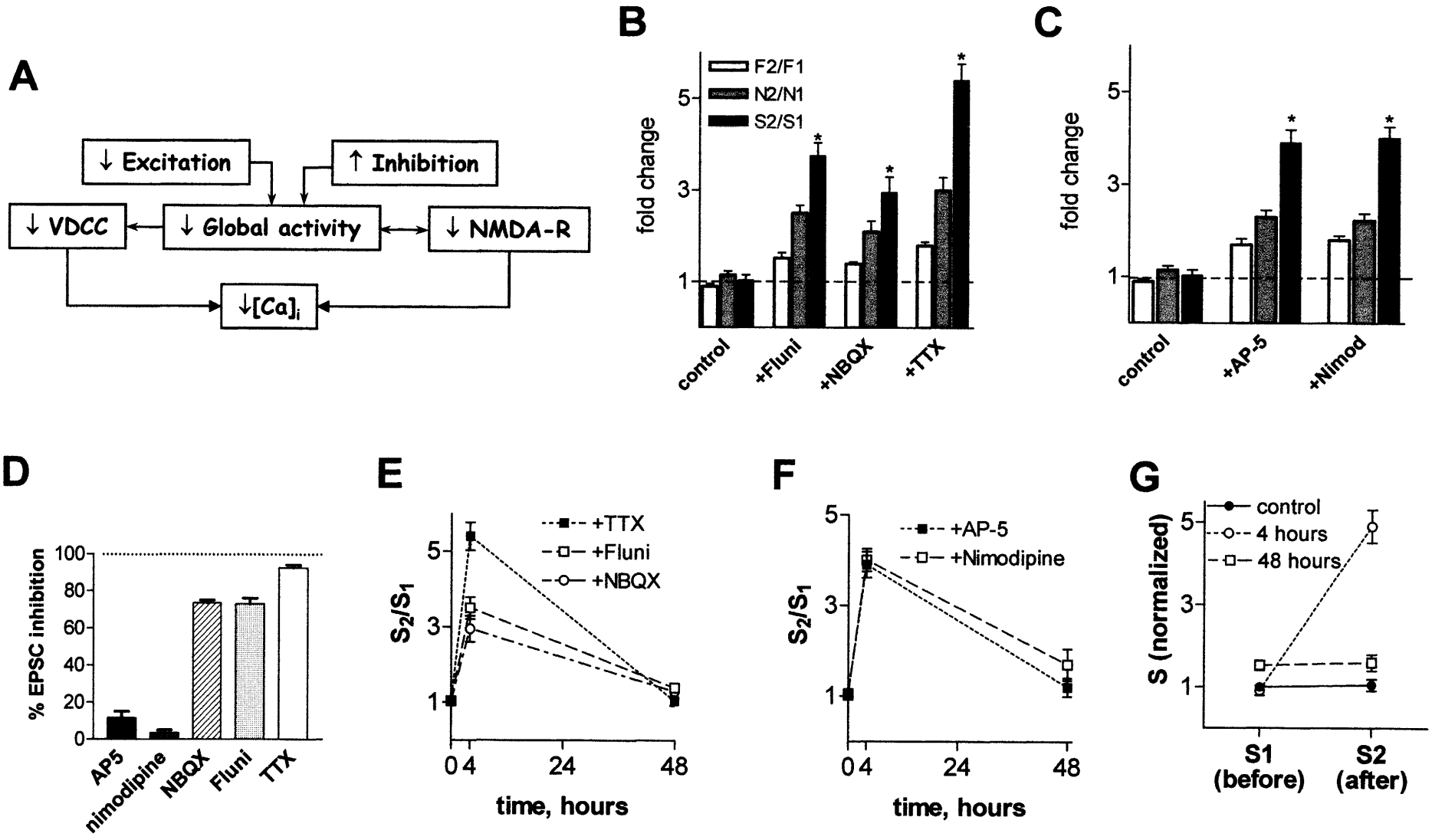
A
↓ Excitation
↑ Inhibition
↓ VDCC
↓ Global activity
↓ NMDA-R
↓[Ca]i
B
F2/F1
N2/N1
S2/S1
fold change
control
+Fluni
+NBQX
+TTX
C
fold change
control
+AP-5
+Nimod
D
% EPSC inhibition
AP5
nimodipine
NBQX
Fluni
TTX
E
+TTX
+Fluni
+NBQX
S2/S1
time, hours
F
+AP-5
+Nimodipine
S2/S1
time, hours
G
control
4 hours
48 hours
S (normalized)
S1 (before)
S2 (after)

Figure 4

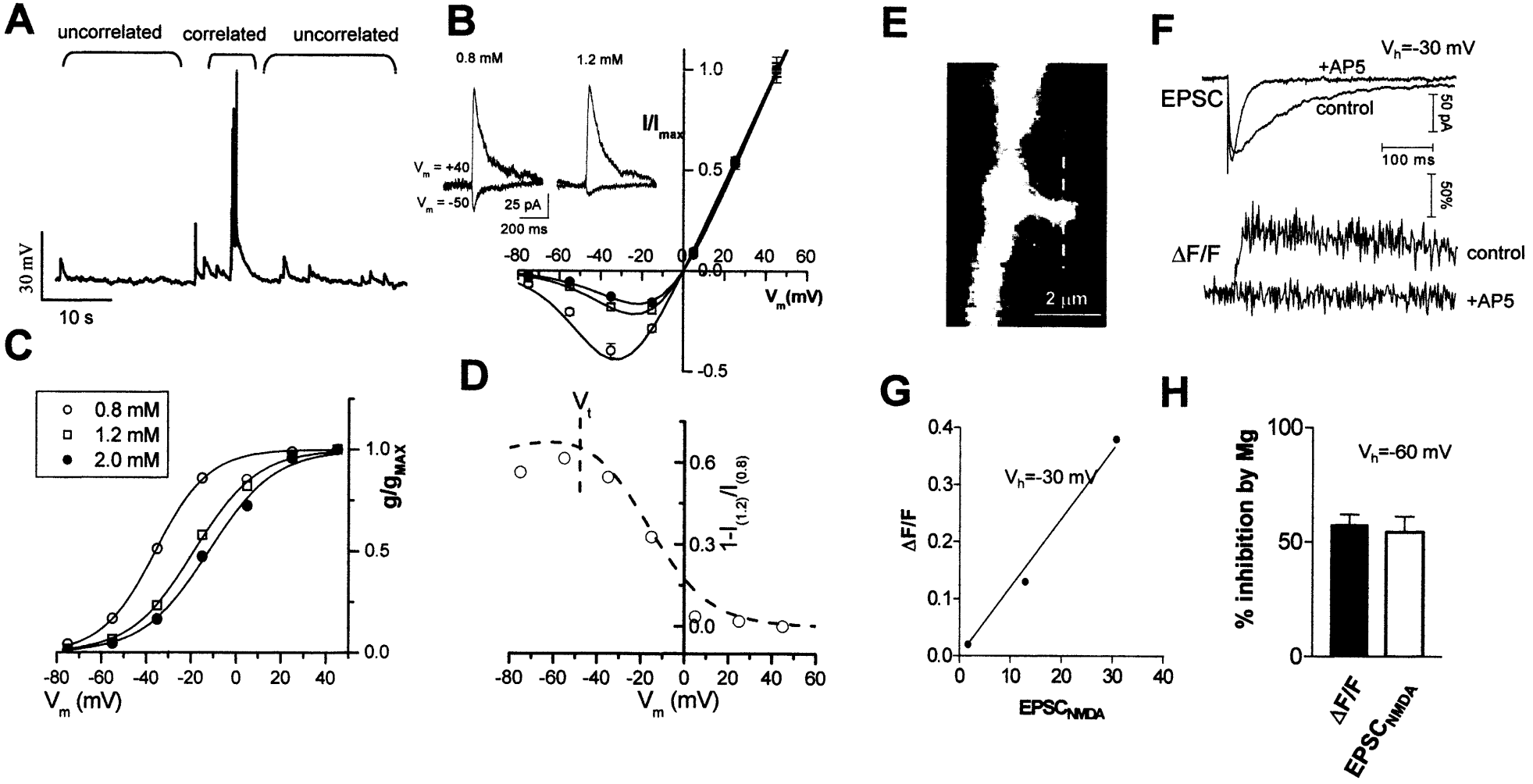
A
uncorrelated
correlated
uncorrelated
30 mV
10 s
B
0.8 mM
1.2 mM
I/I_max
V_m = +40
V_m = -50
25 pA
200 ms
1.0
0.5
0.0
-0.5
-80 -60 -40 -20 0 20 40 60
V_m(mV)
C
0.8 mM
1.2 mM
2.0 mM
g/g_MAX
1.0
0.5
0.0
-80 -60 -40 -20 0 20 40
V_m (mV)
D
V_t
1-I_(1.2)/I_(0.8)
0.6
0.3
0.0
-80 -60 -40 -20 0 20 40 60
V_m (mV)
E
2 μm
F
V_h=-30 mV
+AP5
EPSC
control
50 pA
100 ms
50%
ΔF/F
control
+AP5
G
V_h=-30 mV
ΔF/F
0.4
0.3
0.2
0.1
0.0
0 10 20 30 40
EPSC_NMDA
H
V_h=-60 mV
% inhibition by Mg
100
50
0
ΔF/F
EPSC_NMDA

Figure 5

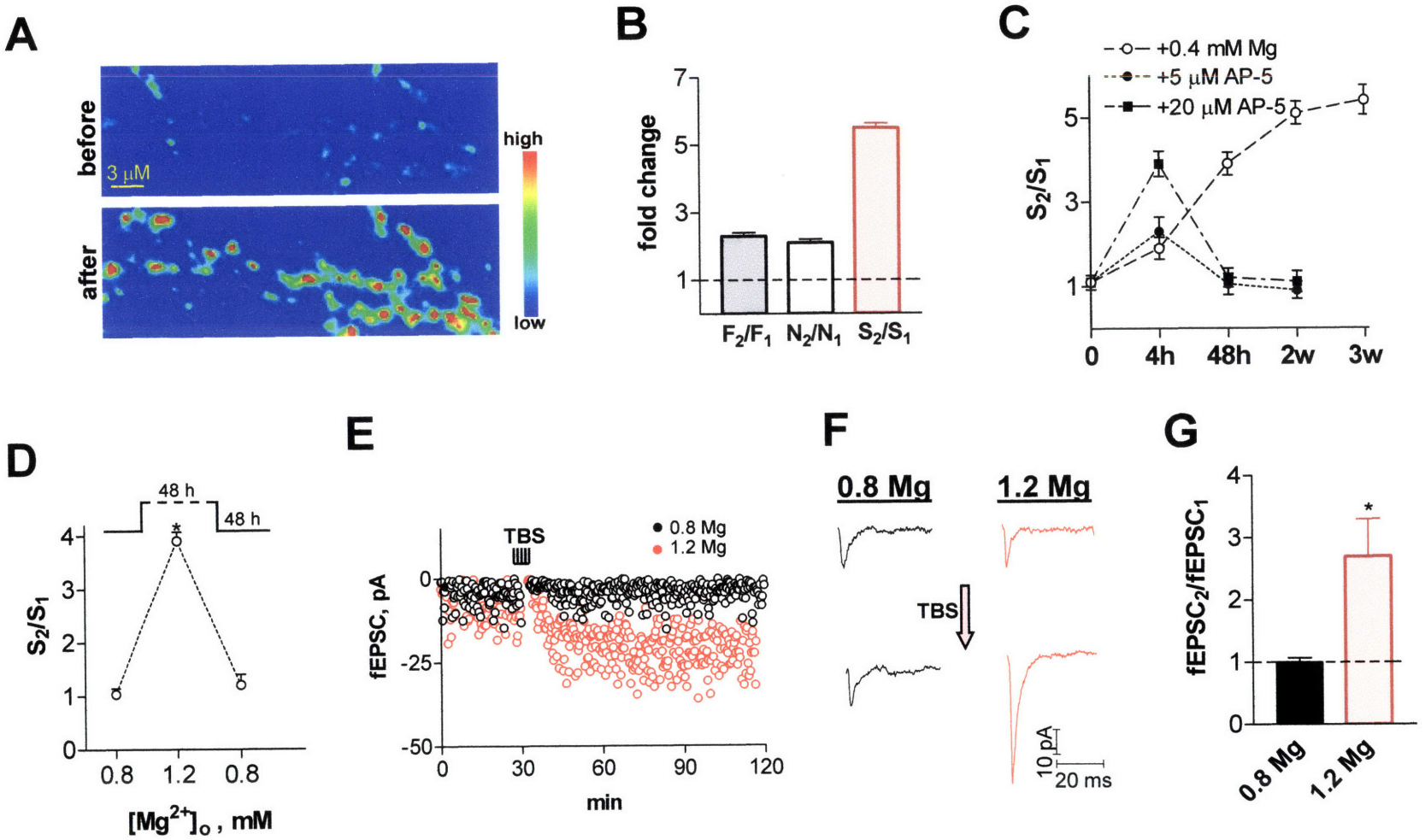
A
before
after
3 μM
high
low
B
fold change
F2/F1
N2/N1
S2/S1
C
+0.4 mM Mg
+5 μM AP-5
+20 μM AP-5
S2/S1
0
4h
48h
2w
3w
D
48 h
48 h
S2/S1
[Mg2+]o , mM
E
TBS
0.8 Mg
1.2 Mg
fEPSC, pA
min
F
0.8 Mg
1.2 Mg
TBS
10 pA
20 ms
G
fEPSC2/fEPSC1
0.8 Mg
1.2 Mg

Figure 6

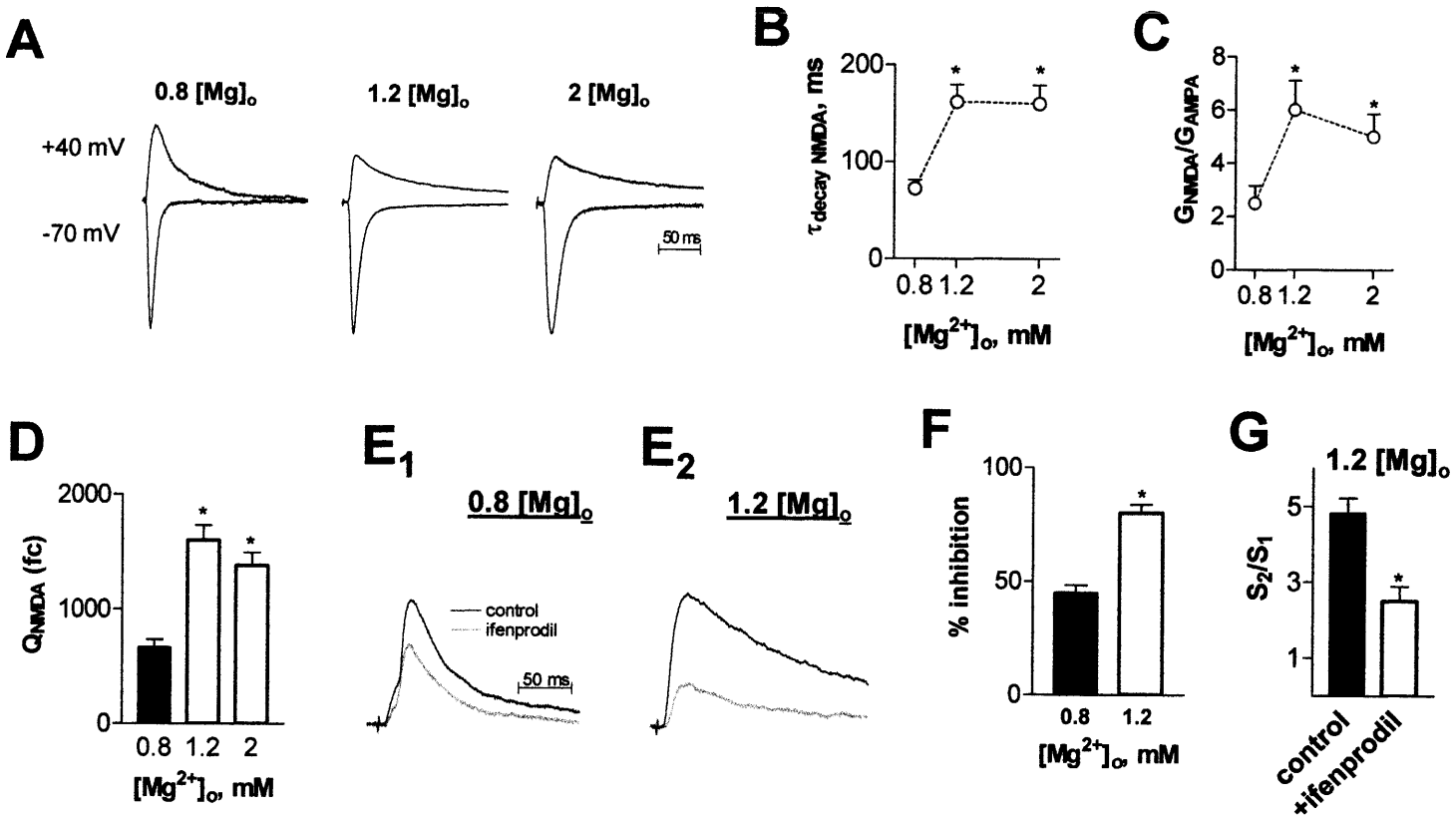
A
0.8 [Mg]o
1.2 [Mg]o
2 [Mg]o
+40 mV
-70 mV
50 ms
B
τdecay NMDA, ms
200
100
0
0.8 1.2 2
[Mg2+]o, mM
C
GNMDA/GAMPA
8
6
4
2
0
0.8 1.2 2
[Mg2+]o, mM
D
QNMDA (fc)
2000
1000
0
0.8 1.2 2
[Mg2+]o, mM
E1
0.8 [Mg]o
control
ifenprodil
50 ms
E2
1.2 [Mg]o
F
% inhibition
100
50
0
0.8 1.2
[Mg2+]o, mM
G
1.2 [Mg]o
S2/S1
5
3
1
control
+ifenprodil

Figure 7

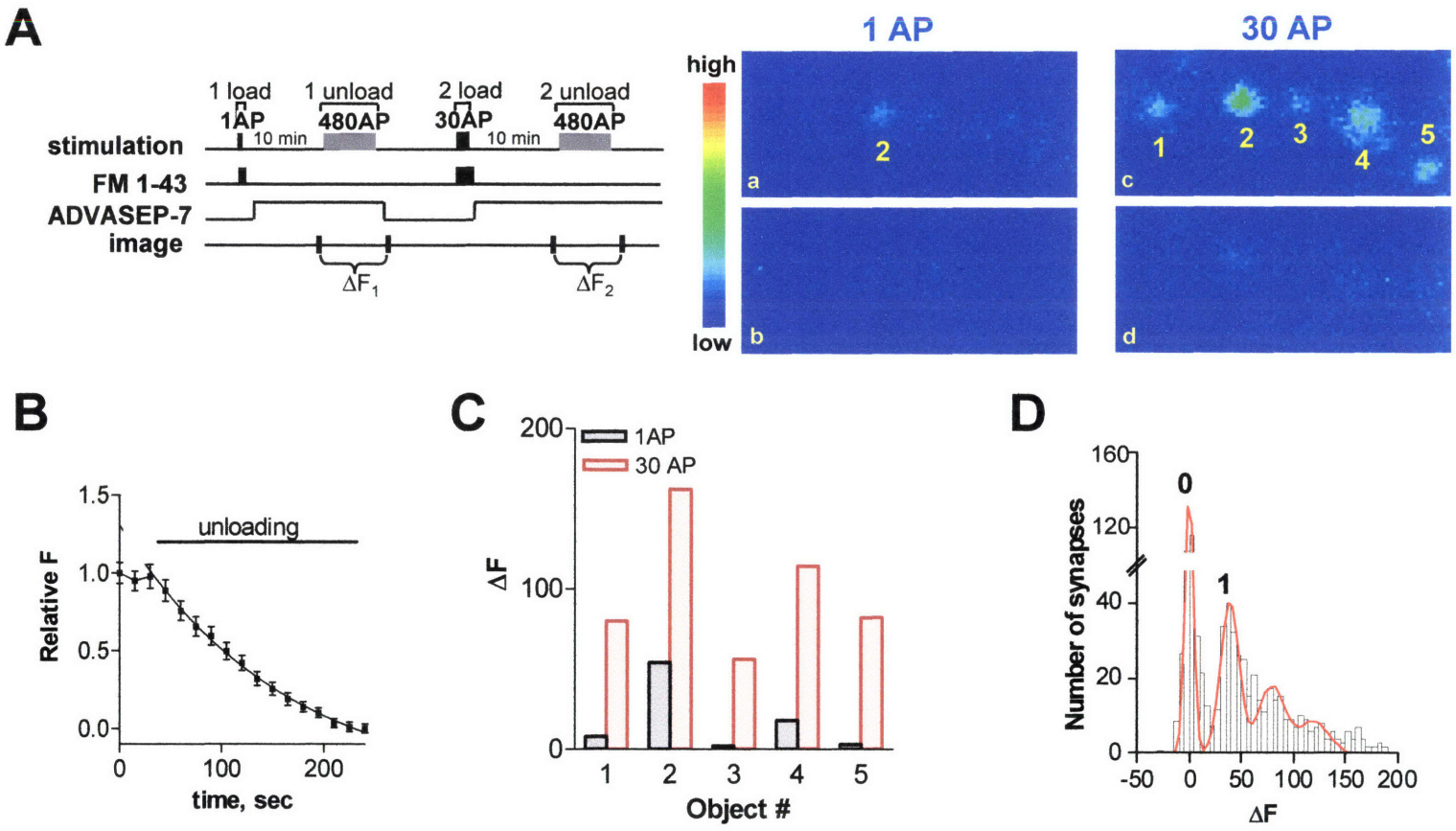
A
1 load
1AP
1 unload
480AP
2 load
30AP
2 unload
480AP
10 min
10 min
stimulation
FM 1-43
ADVASEP-7
image
ΔF1
ΔF2
high
low
1 AP
30 AP
a
b
c
d
2
1
2
3
4
5
B
unloading
Relative F
1.5
1.0
0.5
0.0
0
100
200
time, sec
C
200
100
0
ΔF
1AP
30 AP
1
2
3
4
5
Object #
D
160
120
40
20
0
0
1
Number of synapses
-50
0
50
100
150
200
ΔF

Figure 8

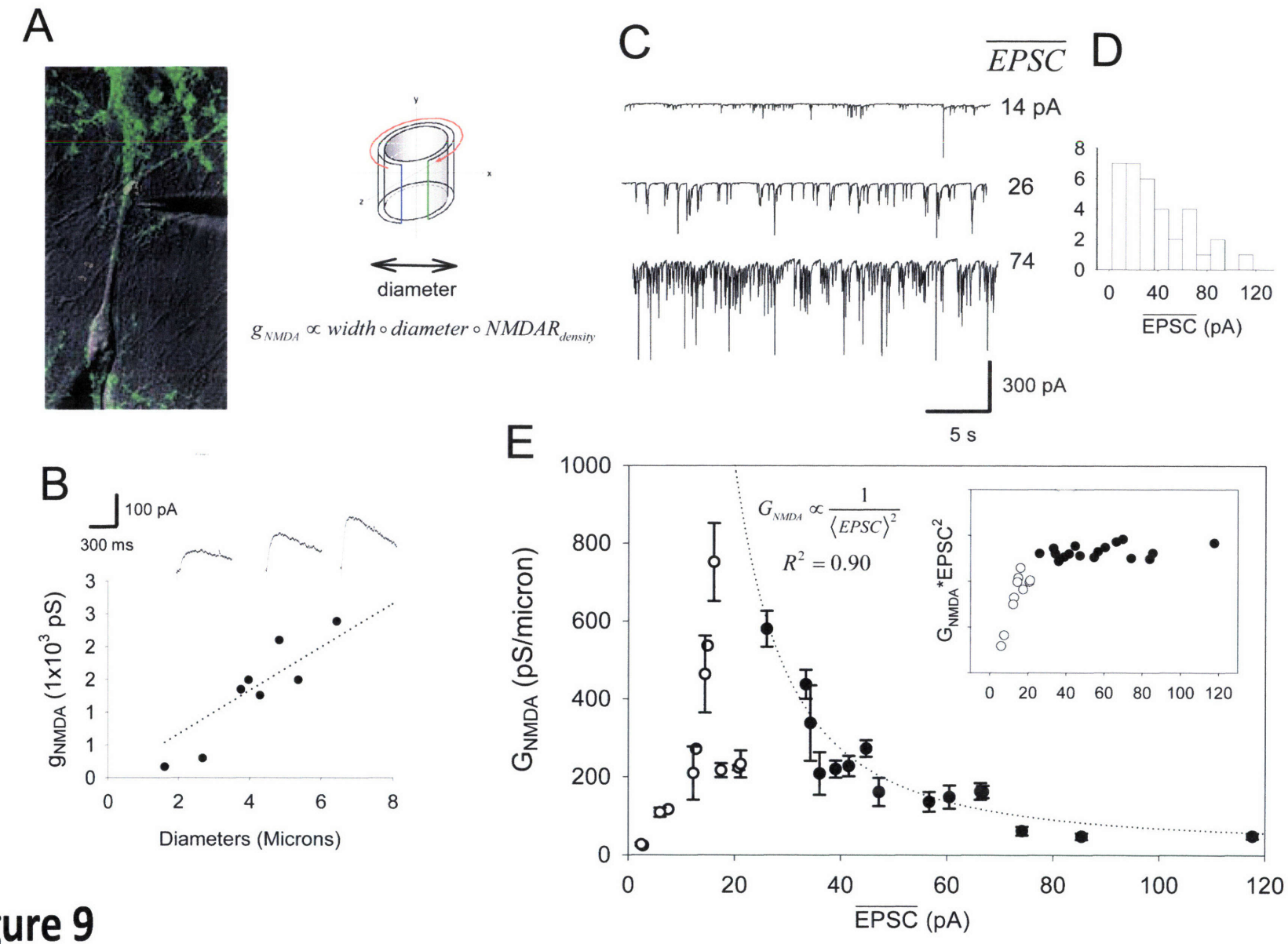
A
diameter
$g_{NMDA} \propto width \circ diameter \circ NMDAR_{density}$
B
100 pA
300 ms
g_{NMDA} (1x10^3 pS)
Diameters (Microns)
C
$\overline{EPSC}$
14 pA
26
74
300 pA
5 s
D
$\overline{EPSC}$ (pA)
E
$G_{NMDA} \propto \frac{1}{\langle EPSC \rangle^2}$
$R^2 = 0.90$
G_{NMDA} (pS/micron)
G_{NMDA}*EPSC^2
$\overline{EPSC}$ (pA)

Figure 9

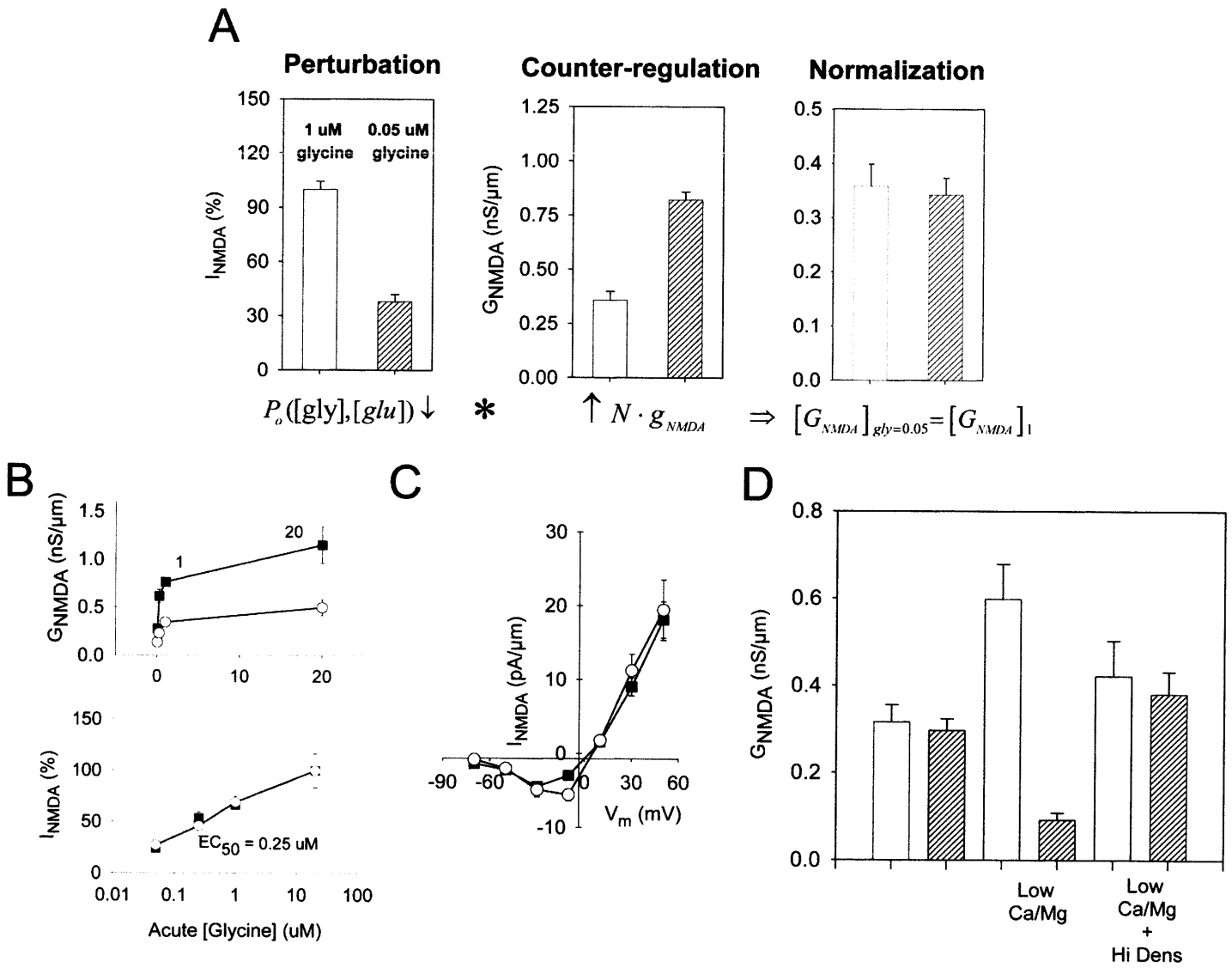
A
Perturbation
Counter-regulation
Normalization
1 uM glycine
0.05 uM glycine
I_{NMDA} (%)
G_{NMDA} (nS/µm)
$P_o([gly],[glu])\downarrow$
*
$\uparrow N \cdot g_{NMDA}$
$\Rightarrow [G_{NMDA}]_{gly=0.05} = [G_{NMDA}]_1$
B
G_{NMDA} (nS/µm)
I_{NMDA} (%)
EC_{50} = 0.25 uM
Acute [Glycine] (uM)
C
I_{NMDA} (pA/µm)
V_m (mV)
D
G_{NMDA} (nS/µm)
Low Ca/Mg
Low Ca/Mg + Hi Dens

Figure 10

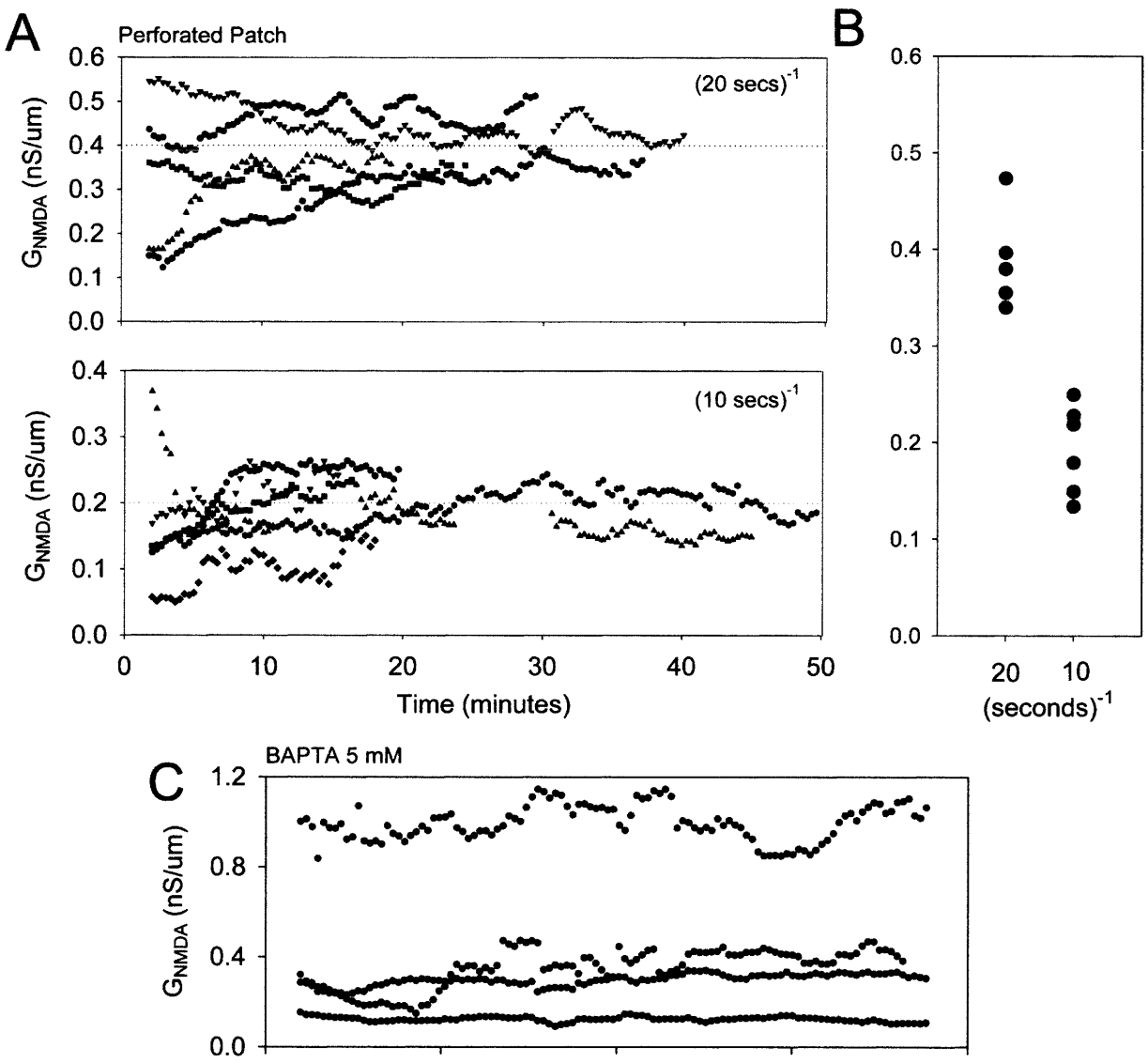
A
Perforated Patch
(20 secs)-1
(10 secs)-1
GNMDA (nS/um)
Time (minutes)
B
20 10
(seconds)-1
C
BAPTA 5 mM
GNMDA (nS/um)

Figure 11

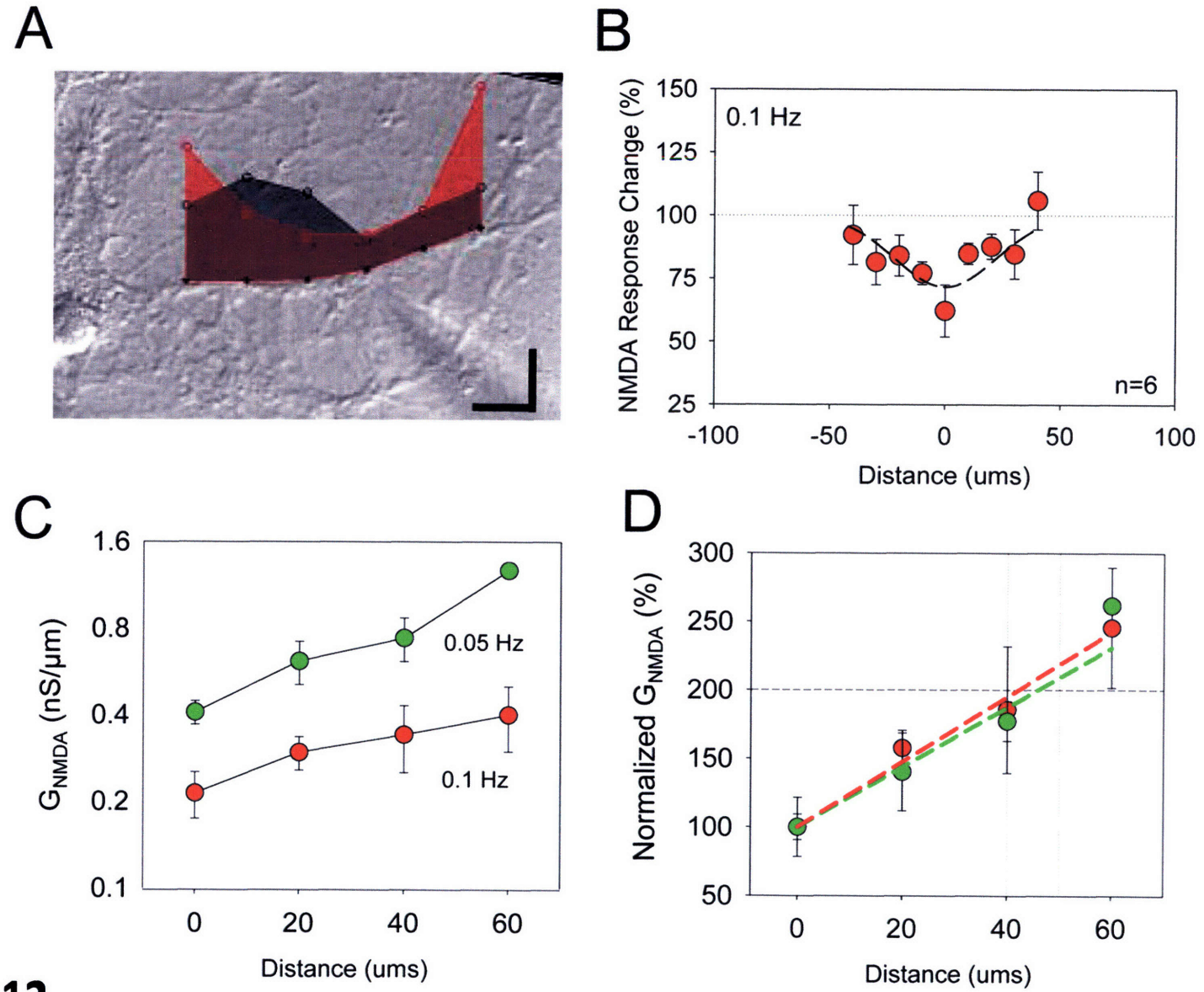
A
B
0.1 Hz
n=6
NMDA Response Change (%)
150
125
100
75
50
25
-100
-50
0
50
100
Distance (ums)
C
D
0.05 Hz
0.1 Hz
G_{NMDA} (nS/µm)
1.6
0.8
0.4
0.2
0.1
0
20
40
60
Distance (ums)
Normalized G_{NMDA} (%)
300
250
200
150
100
50
0
20
40
60
Distance (ums)

Figure 12

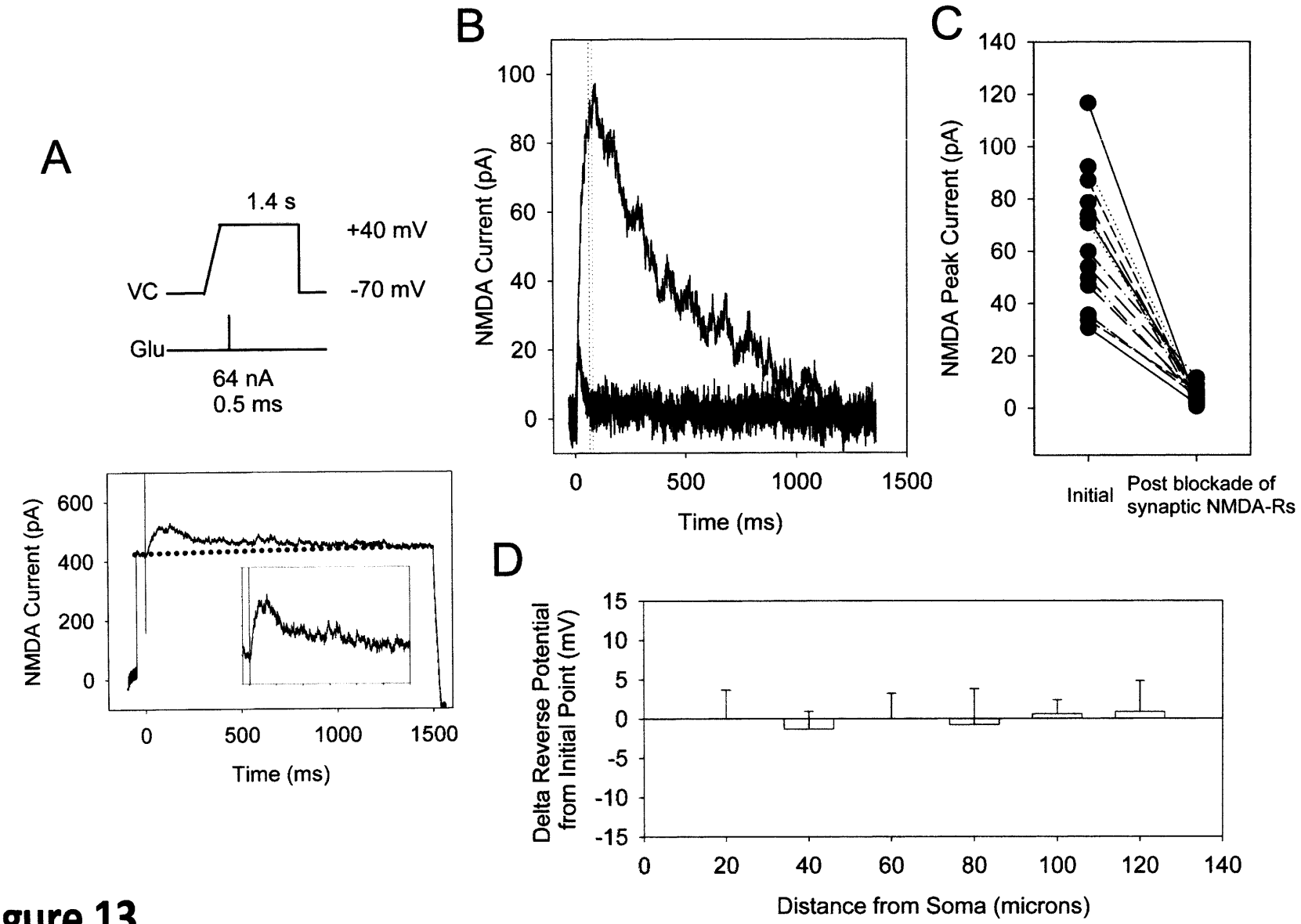
A
1.4 s
+40 mV
VC
-70 mV
Glu
64 nA
0.5 ms
NMDA Current (pA)
600
400
200
0
0
500
1000
1500
Time (ms)
B
NMDA Current (pA)
100
80
60
40
20
0
0
500
1000
1500
Time (ms)
C
NMDA Peak Current (pA)
140
120
100
80
60
40
20
0
Initial
Post blockade of synaptic NMDA-Rs
D
Delta Reverse Potential from Initial Point (mV)
15
10
5
0
-5
-10
-15
0
20
40
60
80
100
120
140
Distance from Soma (microns)

Figure 13

FIGURE LEGENDS

Figure 1. Distribution of Pr in single synapses of hippocampal networks.

(A) Experimental protocol used to determine Pr of presynaptic terminals. (B) Fluorescent images following loading with 30 AP (a), and unloading (b). Fluorescence intensities (arbitrary units) are coded using a pseudocolor transformation shown on the left side of the images. (C) Distribution of ΔF obtained for 30 APs and converted to Pr, using the F_Q=41 value as a conversion factor. Median of Pr is 0.14. (D) Correlation between ΔF_1 and ΔF_2 obtained for two consequent loading-unloading protocols. (E) Fluorescent images obtained following functional labeling with FM 1-43 for 30 AP@1 Hz and 600 AP@20 Hz. Retrospective immunohistochemical staining of the same region revealed that only half of the boutons that were stained with VGLUT1 (for excitatory terminals) or GAD-65 (for inhibitory terminals) correspond to FM-(+) terminals loaded by 30 AP protocol. (F) Comparison between structural and functional synaptic density at various conditions. (G) Co-localization of presynaptic marker VGLUT1, and postsynaptic marker PSD-95.

Figure 2. Reduction of neural activity induces enhancement of synaptic plasticity

(A)Representative fluorescent images, before and 30 minutes after TBS in control (a, b), and TTX-treated (100 nM, 6 hours) (d, e) cultures. DIC images of the same regions (c, f). Fluorescence intensities (arbitrary units) are coded using a pseudocolor transformation shown to the left of the images. (B) Experimental protocol designed to determine ΔF of synapses before and after plasticity induction. TBS (30 bursts, each containing 5 AP@25 Hz, 500 ms inter-burst interval) used as induction protocol. (C) Histograms of ΔF of 704 boutons in control cultures: before (solid lines) and after (dotted lines) TBS from the images, shown in 2A (a, b). There is no change in ΔF distribution in control cultures. (D) Histograms of ΔF 508 boutons in TTX-treated cultures before (solid lines) and after (dotted lines) TBS from the images shown in 2A (d, e). ΔF median increased from 100 to 213, and number of FM detectable boutons increased from 508 to 1608. (E) Plasticity enhancement lasts at least 1.5 hour after TBS induction. (F) Correlation between ΔF of active boutons before and after TBS in control (N=6, blue circles) and TTX-treated (N=5, red circles) cultures. (G) Average magnitude of plasticity (S_2/S_1) for different groups of cultures: 1.1±0.1 for control (N=13), 5.4±0.4 for TTX-treated (N=7), and 1.3±0.2, for TTX-treated in the presence of 50 μM AP-5 during TBS (N=5).

Figure 3. BDNF as a mediator of TBS-induced presynaptic potentiation.

(A) TrkB-IgG (4 μg/ml), applied during TBS, significantly decreases the magnitude of presynaptic potentiation, compared to TTX-treated sister cultures. S_2/S_1 for treated cultures is 5.1±0.5 (N=4) and for treated cultures in the presence of TrkB-IgG is 1.3±0.1 (N=5). (B) Dose-response of Pr to exogenously applied BDNF: (a) BDNF alone (empty circles); (b) BDNF combined with TBS (filled circles) in the presence of cadmium (50 μM) and AP-5, (50 μM) to block pre- and post-synaptic Ca^{2+}-dependent BDNF release in plastic cultures (TTX-treated). EC_{50} for BDNF alone is 25 ng/ml, for BDNF combined with TBS is 2.4 ng/ml. (C_1) Application of BDNF 10 minutes before TBS occludes TBS-induced potentiation (N=3, p>0.3), and (C_2) TBS, applied 10 minutes before BDNF occludes BDNF effect (N=3, p>0.7) in TTX-treated cultures. In both cases BDNF was applied at 20 ng/ml.

Figure 4. Enhancement of plasticity of synaptic terminals by shifting of excitation-inhibition balance or reduction in Ca^{2+} flux

(A) Possible pathways to reduce Ca^{2+} flux in a postsynaptic cell. (B) Enhancing postsynaptic inhibition by 4-6 hours treatment with flunitrazepam (5 μM) or reducing excitation by NBQX (1 μM) induces the up-regulation of synaptic plasticity. S_2/S_1 is 3.8±0.3 (N=4) and 3.0±0.3 (N=4) for flunitrazepam and NBQX, respectively compared to 5.4±0.4 (N=7) for TTX treatment. (C) Short-term (4-6 hours) blockade of NMDAR or L-type VGCC induces enhancement of the plasticity of presynaptic terminals. Average results of treatment with AP-5 (20 μM) and nimodipine (10 μM) for the magnitude of synaptic plasticity: S_2/S_1 is 3.9±0.3 (N=4) and 4.0±0.5 (N=4) for AP-5 and nimodipine, respectively. (D) Effects of AP-5 (20 μM), nimodipine (10 μM), NBQX (1 μM), flunitrazepam (5 μM), and TTX (100nM) on neuronal activity, expressed as an integral of EPSCs at –60 mV. (E) Synaptic terminals lose plasticity after prolonged reduction of neural activity with TTX (N=5), NBQX (N=5) and flunitrazepam (N=8). (F) Chronic incubation for 48 hours with AP-5 (N=6) and nimodipine (N=4) does not trigger an increase of synaptic plasticity. (G) Comparison of presynaptic strength before (S_1) and after (S_2) TBS in control, 4 and 48 hours TTX-treated cultures. Short-term (4 hours) application of TTX did not significantly change initial presynaptic strength (S_1) ($p>0.5$, N=5). Long-term (48 hours) incubation induced 1.5 (±0.1)-fold increase in S_1 ($p<0.005$, N=6), which is significantly lower than the maximal TBS-induced potentiation (S_2=4.9±0.4, N=6). S values were normalized by S_1 of control cultures.

Figure 5. Voltage-dependent NMDA channel opening is sensitive to physiological variation in $[Mg^{2+}]_o$

(A) Exemplary membrane potential trace recorded under current clamp showing uncorrelated (background) and correlated (bursting) patterns of neuronal activity. (B) Normalized peak glutamate-activated NMDA currents plotted against membrane potential in three $[Mg^{2+}]_o$ (0.8 (○), 1.2 (□), and 2.0 mM (●)). Membrane potentials were varied from -70 to +50 mV in 20 mV increments and currents were recorded from cultured CA1 pyramidal neurons (N = 5). Since the evoked NMDA currents varied among the synapses examined, the amplitudes of NMDA currents were normalized to their maximum values to group all data points together. (C) Normalized g-V relationship, where g/g_{max} was the peak conductance of NMDA channel at 0.8 (○), 1.2 (□) and 2 mM (●) $[Mg^{2+}]_o$. The continuous lines through points were obtained by fitting g-V relationship with Eqn (1) with the parameters ? and K_{Mg}. (D) The fraction of NMDAR Mg^{2+} block at 1.2 mM $[Mg^{2+}]_o$ relating to 0.8 $[Mg^{2+}]_o$ as a function of membrane potential. Note the ~60% greater attenuation of NMDA current at the sub-threshold range of membrane potential with 1.2 mM $[Mg^{2+}]_o$ and the decline of this effect when membrane potential crosses the threshold for action potential generation (marked as V_t). (E) Dendritic spine visualized with Alexa 633. (F) The time course of NMDA currents and associated Ca^{2+}-dependent fluorescence transients ($\Delta F/F$, n=3) in controls and following application of AP-5 (50 μM) from the spine depicted in (E). (G) The amplitude of NMDA currents and Ca^{2+} influx ($\Delta F/F$) at a single spine are linearly correlated

(r^2=0.99). (H) Elevation of $[Mg^{2+}]_o$ from 0.8 mM to 1.2 mM led to a parallel reduction of NMDA currents (57±5 %) and Ca^{2+} influx (54±7 %) (n = 3, Vm = -60 mV).

Figure 6. Long-term elevation of $[Mg^{2+}]_o$ enables synapses to remain highly plastic

(A) Representative fluorescent images before and 30 minutes after TBS in Mg^{2+}-treated (for 2 weeks) hippocampal culture. (B) Quantification of changes induced by TBS stimulation: ($\Delta F_2/\Delta F_1 = 2.3 \pm 0.1$ (gray bar), $N_2/N_1 = 2.1 \pm 0.1$ (white bar), $S_2/S_1 = 5.5 \pm 0.2$ (red bar), N=15). (C) Time-course of enhancement of synaptic plasticity induced by 0.4 mM Mg^{2+} (○), 5 μM AP-5 (●) and 20 μM AP-5 (■).(D) Mg^{2+}-induced enhancement of plasticity is reversible. Elevation of $[Mg^{2+}]_o$ from 0.8 to 1.2 mM for 48 hours induced the enhancement of synaptic plasticity (the same data as in Figure 6C) and subsequent reduction of $[Mg^{2+}]_o$ back to 0.8 mM for 48 hours returned the terminals to a non-plastic state ($S_2/S_1 = 1.1 \pm 0.2$, N=3, $p>0.2$). (E) The peak amplitude of fEPSC before and after LTP induction by TBS. Black circle: recording from neuron in 0.8 mM $[Mg^{2+}]_o$ cultures; Red circle: in 1.2 mM $[Mg^{2+}]_o$ cultures. (F) Representative traces of EPSC before and 30 minutes after TBS induction in 0.8 (black traces) and 1.2 (red traces) mM $[Mg^{2+}]_o$ cultures. (G) Average results of TBS-induced modification of EPSC: $fEPSC_2/fEPSC_1$ is 1.0 ± 0.1 (N=4) and 2.7 ± 0.6 (N=5), in 0.8 (black bar) and 1.2 (red bar) mM $[Mg^{2+}]_o$ cultures respectively.

Figure 7. The long-term effects of elevation of $[Mg^{2+}]_o$ on the $EPSC_{NMDA}$.

(A) Recordings of evoked EPSCs at -70 mV and +40 mV (in the presence of 50 μM picrotoxin) between pairs of neurons in control (0.8), 1.2 and 2 mM Mg^{2+} cultures. (B) The decay time-constant (τ_{decay}) of $EPSC_{NMDA}$ as function of $[Mg^{2+}]_o$. (C) N/A ratio (calculated as an integral of G_{NMDA}/G_{AMPA}) at different $[Mg^{2+}]_o$. (D) The charge transfer of quantal $EPSC_{NMDA}$ ($Q_{NMDA\ (-70mV)}$) as a function of $[Mg^{2+}]_o$. (E) Recordings of $EPSC_{NMDA}$ (in the presence of 1 μM NBQX and 50 μM picrotoxin) in control conditions and after application of 3 μM of ifenprodil in neurons from 0.8 and 1.2 mM Mg^{2+} cultures. The peak amplitudes of EPSC during control recordings were normalized to allow for the comparison of drug sensitivity. (F) Ifenprodil has stronger inhibitory effects on $EPSC_{NMDA}$ in neurons from 1.2 mM $[Mg^{2+}]_o$ cultures (0.8 mM: 45 ± 2 %, N=6, $p<0.01$; 1.2 mM: 80% ± 4, N=5, $p<0.001$). (G) 1 μM ifenprodil (IC_{50}) reduced TBS-induced presynaptic potentiation by 48 ± 7 % in 1.2 mM Mg^{2+} cultures (N=4, $p<0.005$).

Figure 8. Determination of single vesicle fluorescence, F_Q.

(A) Experimental protocol used to determine Pr of presynaptic terminals (left). The right panel shows fluorescent images of the same region following loading with 1 AP (a), first unloading (b), loading with 30 AP (c), and second unloading (d). (B) Decay of average intensity of the fluorescent puncta during unloading using 2 Hz stimulation. Each point represents an average of 841 boutons. (C) Comparison of ΔF in terminals loaded by 1 (gray bars) and 30 APs (red bars) shown in 1A. (D) Histogram of ΔF in terminals stained with 1 APs from one experiment. The red curve represents the best fit to sum of four Gaussian distributions with quantal spacing, F_Q=39.8 (see Experimental procedures). The first peak represents boutons that did not release vesicles at all; the second peak represents terminals that released one vesicle.

Figure 9. Synaptic Input Determines Functional NMDA Density. A. High-resolution glutamatergic iontophoresis applied simultaneous with perforated whole-cell recording. FM-143 has here been used to shown pre-synaptic terminals (green). B. NMDA conductance at different dendritic locations covaries linearly with dendritic diameter in single neuron. (R^2=0.93) C. Three examples of synaptic input recorded from neurons in voltage clamp. Each cell was recorded for 3-10 minutes. Baseline leak current was subtracted and average current input over time was calculated ($\overline{EPSC}$). D. Histogram of input distribution shows wide heterogeneity. E. Synaptic Input predicts functional NMDA Density. Best fit with $k/\langle EPSC \rangle^2$ generates R^2=0.90 (n = 35 neurons; threshold of ~25 pA; an inverse first power fit produced a weaker R^2=0.74). Inset shows a log-linear plot of putative NMDA activation over time (G_{NMDA} *EPSC^2) versus average synaptic input. Note that when $\overline{EPSC}$ > 25 pA, averaged NMDA current flux over time is constant despite the variation of synaptic inputs.

Figure 10. Glycine Perturbation Causes NMDA Normalization. A. Acute effect of two extra-cellular glycine concentrations on NMDA currents (left panel). Ratio of recordings conducted on same dendritic locations = 2.63 ± 0.35 (n=4 neurons/N=9 synaptic locations). Lower glycine concentration leads to precisely matched chronic up-regulation of NMDA functional density (middle). Ratio = 2.29±0.10 (n/N=7/22 for 1 uM, n/N = 3/9 for 50 nM) all cultures chronically treated for 4-6 hours in ACSF with appropriate glycine concentration and then tested in 1 uM glycine + TTX. Quantitative NMDA Normalization across two treatment conditions (right). G_{NMDA} for neurons treated and tested in 1 uM glycine = 358 ± 41 $pS/\mu m$ (n/N=7/25) and for those treated and tested in 50 nM = 342 ± 31 $pS/\mu m$, (n/N=7/22; t-test p= 0.76) B and C. Glycine sensitivity and voltage-dependence are unchanged after NMDA Normalization. D. NMDA normalization breaks down at low activity levels and is rescued with increased neuronal density. 1 uM glcyine (white) and 50 nM (hatched) comparison groups in standard ([Ca/Mg]=1.2/0.8) conditions show NMDA normalization as described in 2A. A ~4-fold reduction in extracellular ([Ca/Mg]= 0.6/1.6,1 uM glycine) leads to expected increase in functional NMDA density (G_{NMDA} = 599±81 $pS/\mu m$ (n/N=5/24), p < 0.05, white, third bar from left). Further decreasing glycine to 50 nM causes G_{NMDA} to decrease rather than increase (hatched, fourth bar from left). In the low Ca/Mg case, the functional NMDA density between glycine groups is statistically different ($G_{NMDA(1\mu M)}$ = 599±81 $pS/\mu m$ (n/N=5/24) and $G_{NMDA(50nM)}$ = 92 +/- 16 $pS/\mu m$ (n/N=4/10), p < 0.001; second pair of bars from left). Increasing plating neuronal density by 50% rescues NMDA normalization

causing the glycine treatment groups to again become statistically indistinguishable ($G_{NMDA(1\mu M)}$ =421±82 $pS/\mu m$ (n/N=4/10) and $G_{NMDA(50nM)}$ = 380±51 $pS/\mu m$ (n/N=4/12), p=0.66; third pair of bars from left).

Figure 11. Frequency of NMDAR activation Determines NMDA Functional Density. A. Standard technique used to measure local NMDA responsiveness is repeated over time to generate sustained local NMDA activation over time. ([Ca/Mg] =1.2/0.8 mM; glycine=1uM in the presence of 0.5 uM TTX and 10 nM nimodipine). To avoid intermixing results from neurons in putatively different states, the cells studied were chosen among those that were above the synaptic activity threshold shown in Figure 1. B. Doubling of NMDAR activation leads to halving of functional NMDA density. Note that despite of difference in initial NMDAR densities, the final values were scaled respective to the frequency of activation (G_{NMDA} = 389±23; 0.05 Hz and 199 ± 18.8 *pS/μm*; 0.1 Hz; $p < 0.0001$; N=5 and 6 neurons). C. Intra-cellular BAPTA leads to stable NMDA recordings (initial = 408±190; final = 479±202 *pS/μm*).

Figure 12. NMDA Normalization is Spatially Local. A. Representative case of one neuron. Initial G_{NMDA} distribution (black profile) and G_{NMDA} distribution after $(10 \text{ seconds})^{-1}$ modification protocol (red profile). Height of profile away from dendrite denotes magnitude of peak NMDA flux. Scale bars - vertical (25 pA) and horizontal (20 ums). B. Relative decrease in functional NMDA Density is spatially limited (initial G_{NMDA} = 316 +/- 73 $pS/\mu m$. t-test comparing samples at point of glutamate release versus grouped values at both 30 and 40 microns, $p<0.05$, best-fit Gaussian of the points R = 0.42), C. G_{NMDA} distribution after long-term stimulation shows monotonic increase with distance from point of focal glutamate delivery (n=8 and 5 for 0.1 Hz and 0.05 Hz respectively). Note that in this panel the spatial step size used was 20 microns instead of 10 microns. D. G_{NMDA} doubles ($\lambda_{1/2}$) roughly at ~ 40-50 ums regardless of which stimulation frequency is used (best-linear fit R=0.80 and cross-point = 46 microns for 0.05 Hz and R=0.58 and cross-point = 42 microns for 0.1 Hz; t-test comparisons between edges and point of glutamate delivery, mean G_{NMDA} for 0.1 Hz at 60 microns divided by G_{NMDA} at point of glutamate delivery = 246 ± 44% with t-test $p < 0.01$ and for 0.05 Hz at, due to limited n, grouped 40 and 60 microns samples = 194 ± 20% with t-test $p < 0.01$).

Figure 13. A. Method for determining local NMDA responsiveness. Depolarization to +40 mV for 1.4 seconds leads to a linear baseline on which one observes super-positioned outward AMPA and NMDA currents. Substraction of the trendline yields NMDA and AMPA components (inset). B and C. High-resolution iontophoresis activates NMDA receptors which are the same as those activated endogenously. We use an averaging time window to dissociate the NMDA and AMPA responses generated by glutamate release (15 ms averaging window starting at 65 ms after glutamate release) (Watt et al., 2000). When an AMPA-R antagonist is applied (i.e. NBQX), this averaged response within the window is unaffected, when an NMDA-R antagonist is applied (i.e. 7-Chlorokynurenic acid), it is completely abolished (data not shown). We wished to determine whether the stimulated NMDA-R population corresponds to that activated with synaptic release of glutamate. Thus, we used a technique that combines intra-cellular BAPTA (5 mM) to block NMDA-receptor desensitization, biccucculine (50 uM) to induce network bursting, and MK-801 (10 uM) to block only those NMDA channels opened by synaptic release of glutamate (Hardingham & Bading, 2003). Afterwards, biccucculine and MK-801 are washed out. Sampling of NMDA currents before and after such a protocol reveals that the overwhelming majority of iontophoretically generated NMDA response corresponds to synaptically activated receptors (>95% of initial current is abolished; 4 neurons, 15 dendritic locations, t-test $p < 1e\text{-}9$). This is likely due to the high packing density of synapses on the dendrites of excitatory neurons (2-3 synapses / micron)(Slutsky et al., 2004a). Thus, iontophoretic generated NMDA responses closely represent the NMDA-R population activated by synaptic release. (Slutsky, Sadeghpour,

Li, & Liu, 2004b). D. The reversal potential of NMDA receptors is unchanged within the first 120 microns of dendrite. Repeat measurement of the NMDA-R reversal potential at multiple dendritic sites demonstrates that it is the same at all points (n=5 neurons). This suggests that the spatial clamp is appropriate and permits us to interpret the spatial mapping experiments shown in Figure 4 as representing actual NMDA receptor availability.

Table 1. Woodhull parameters for voltage dependency of Mg^{2+} block as a function of $[Mg^{2+}]_o$.

$[Mg^{2+}]_o$ (mM)	K_{Mg} (mM)	?	n
0.8	16.3±1.0	1.00±0.02	5
1.2	4.5 ±0.3	0.90±0.03	5
2.0	4.5 ±0.4	0.87±0.06	5

Bibliography

Abraham, W. C., & Bear, M. F. (1996). Metaplasticity: the plasticity of synaptic plasticity. *Trends Neurosci, 19*(4), 126-130.

Allen, C., & Stevens, C. F. (1994). An evaluation of causes for unreliability of synaptic transmission. *Proc Natl Acad Sci U S A, 91*(22), 10380-10383.

Aravanis, A. M., Pyle, J. L., & Tsien, R. W. (2003). Single synaptic vesicles fusing transiently and successively without loss of identity. *Nature, 423*(6940), 643-647.

Bacci, A., Coco, S., Pravettoni, E., Schenk, U., Armano, S., Frassoni, C., et al. (2001). Chronic blockade of glutamate receptors enhances presynaptic release and downregulates the interaction between synaptophysin-synaptobrevin-vesicle-associated membrane protein 2. *J Neurosci, 21*(17), 6588-6596.

Baddeley, R., Abbott, L. F., Booth, M. C., Sengpiel, F., Freeman, T., Wakeman, E. A., et al. (1997). Responses of neurons in primary and inferior temporal visual cortices to natural scenes. *Proc Biol Sci, 264*(1389), 1775-1783.

Bear, M. F. (2003). Bidirectional synaptic plasticity: from theory to reality. *Philos Trans R Soc Lond B Biol Sci, 358*(1432), 649-655.

Betz, W. J., Mao, F., & Bewick, G. S. (1992). Activity-dependent fluorescent staining and destaining of living vertebrate motor nerve terminals. *J Neurosci, 12*(2), 363-375.

Bi, G. Q., & Poo, M. M. (1998). Synaptic modifications in cultured hippocampal neurons: dependence on spike timing, synaptic strength, and postsynaptic cell type. *J Neurosci, 18*(24), 10464-10472.

Bliss, T. V., & Collingridge, G. L. (1993). A synaptic model of memory: long-term potentiation in the hippocampus. *Nature, 361*(6407), 31-39.

Boulanger, L., & Poo, M. M. (1999). Presynaptic depolarization facilitates neurotrophin-induced synaptic potentiation. *Nat Neurosci, 2*(4), 346-351.

Buonomano, D. V., & Merzenich, M. M. (1998). Cortical plasticity: from synapses to maps. *Annu Rev Neurosci, 21*, 149-186.

Burgoyne, R. D., O'Callaghan, D. W., Hasdemir, B., Haynes, L. P., & Tepikin, A. V. (2004). Neuronal Ca2+-sensor proteins: multitalented regulators of neuronal function. *Trends Neurosci, 27*(4), 203-209.

Carmignoto, G., & Vicini, S. (1992). Activity-dependent decrease in NMDA receptor responses during development of the visual cortex. *Science, 258*(5084), 1007-1011.

Cash, S., & Yuste, R. (1999). Linear summation of excitatory inputs by CA1 pyramidal neurons. *Neuron, 22*(2), 383-394.

Chang, E. F., & Merzenich, M. M. (2003). Environmental noise retards auditory cortical development. *Science, 300*(5618), 498-502.

Chutkow, J. G. (1974). Metabolism of magnesium in central nervous system. Relationship between concentrations of magnesium in cerebrospinal fluid and brain in magnesium deficiency. *Neurology, 24*(8), 780-787.

Cline, H. T., Debski, E. A., & Constantine-Paton, M. (1987). N-methyl-D-aspartate receptor antagonist desegregates eye-specific stripes. *Proc Natl Acad Sci U S A, 84*(12), 4342-4345.

Colonnese, M. T., Zhao, J. P., & Constantine-Paton, M. (2005). NMDA receptor currents suppress synapse formation on sprouting axons in vivo. *J Neurosci, 25*(5), 1291-1303.

Engert, F., & Bonhoeffer, T. (1997). Synapse specificity of long-term potentiation breaks down at short distances. *Nature, 388*(6639), 279-284.

Engert, F., & Bonhoeffer, T. (1999). Dendritic spine changes associated with hippocampal long-term synaptic plasticity. *Nature, 399*(6731), 66-70.

Fagiolini, M., Katagiri, H., Miyamoto, H., Mori, H., Grant, S. G., Mishina, M., et al. (2003). Separable features of visual cortical plasticity revealed by N-methyl-D-aspartate receptor 2A signaling. *Proc Natl Acad Sci U S A, 100*(5), 2854-2859.

Fagiolini, M., Pizzorusso, T., Berardi, N., Domenici, L., & Maffei, L. (1994). Functional postnatal development of the rat primary visual cortex and the role of visual experience: dark rearing and monocular deprivation. *Vision Res, 34*(6), 709-720.

Flint, A. C., Maisch, U. S., Weishaupt, J. H., Kriegstein, A. R., & Monyer, H. (1997). NR2A subunit expression shortens NMDA receptor synaptic currents in developing neocortex. *J Neurosci, 17*(7), 2469-2476.

Forsythe, I. D., Westbrook, G. L., & Mayer, M. L. (1988). Modulation of excitatory synaptic transmission by glycine and zinc in cultures of mouse hippocampal neurons. *J Neurosci, 8*(10), 3733-3741.

Fox, K. (1992). A critical period for experience-dependent synaptic plasticity in rat barrel cortex. *J Neurosci, 12*(5), 1826-1838.

Franks, K. M., & Isaacson, J. S. (2005). Synapse-specific downregulation of NMDA receptors by early experience: a critical period for plasticity of sensory input to olfactory cortex. *Neuron, 47*(1), 101-114.

Frick, A., Magee, J., & Johnston, D. (2004). LTP is accompanied by an enhanced local excitability of pyramidal neuron dendrites. *Nat Neurosci, 7*(2), 126-135.

Gilbert, C. D., Sigman, M., & Crist, R. E. (2001). The neural basis of perceptual learning. *Neuron, 31*(5), 681-697.

Goebel, D. J., & Poosch, M. S. (1999). NMDA receptor subunit gene expression in the rat brain: a quantitative analysis of endogenous mRNA levels of NR1Com, NR2A, NR2B, NR2C, NR2D and NR3A. *Brain Res Mol Brain Res, 69*(2), 164-170.

Goldberg, J., Holthoff, K., & Yuste, R. (2002). A problem with Hebb and local spikes. *Trends Neurosci, 25*(9), 433-435.

Groc, L., Gustafsson, B., & Hanse, E. (2003). In vivo evidence for an activity-independent maturation of AMPA/NMDA signaling in the developing hippocampus. *Neuroscience, 121*(1), 65-72.

Groc, L., Heine, M., Cognet, L., Brickley, K., Stephenson, F. A., Lounis, B., et al. (2004). Differential activity-dependent regulation of the lateral mobilities of AMPA and NMDA receptors. *Nat Neurosci, 7*(7), 695-696.

Hardingham, G. E., & Bading, H. (2003). The Yin and Yang of NMDA receptor signalling. *Trends Neurosci, 26*(2), 81-89.

Hardingham, G. E., Fukunaga, Y., & Bading, H. (2002). Extrasynaptic NMDARs oppose synaptic NMDARs by triggering CREB shut-off and cell death pathways. *Nat Neurosci, 5*(5), 405-414.

Heinrich, J. E., Singh, T. D., Nordeen, K. W., & Nordeen, E. J. (2003). NR2B downregulation in a forebrain region required for avian vocal learning is not sufficient to close the sensitive period for song learning. *Neurobiol Learn Mem, 79*(1), 99-108.

Hodgkin, A. L., & Huxley, A. F. (1952). A quantitative description of membrane current and its application to conduction and excitation in nerve. *Journal of Physiology, 117*, 500-544.

InstituteofMedicine. (1997). *Dietary reference intakes of calcium, phosphorus, magnesium, vitamin D, and fluoride*. Washington, D.C: National Academic Press.

Jackson, M. E., Homayoun, H., & Moghaddam, B. (2004). NMDA receptor hypofunction produces concomitant firing rate potentiation and burst activity reduction in the prefrontal cortex. *Proc Natl Acad Sci U S A, 101*(22), 8467-8472.

Jahr, C. E., & Stevens, C. F. (1990). A quantitative description of NMDA receptor-channel kinetic behavior. *J Neurosci, 10*(6), 1830-1837.

Jahr, C. E., & Stevens, C. F. (1993). Calcium permeability of the N-methyl-D-aspartate receptor channel in hippocampal neurons in culture. *Proc Natl Acad Sci U S A, 90*(24), 11573-11577.

Kang, H., Welcher, A. A., Shelton, D., & Schuman, E. M. (1997). Neurotrophins and time: different roles for TrkB signaling in hippocampal long-term potentiation. *Neuron, 19*(3), 653-664.

Kapaki, E., Segditsa, J., & Papageorgiou, C. (1989). Zinc, copper and magnesium concentration in serum and CSF of patients with neurological disorders. *Acta Neurol Scand, 79*(5), 373-378.

Katz, L. C., & Shatz, C. J. (1996). Synaptic activity and the construction of cortical circuits. *Science, 274*(5290), 1133-1138.

Kay, A. R., Alfonso, A., Alford, S., Cline, H. T., Holgado, A. M., Sakmann, B., et al. (1999). Imaging synaptic activity in intact brain and slices with FM1-43 in C. elegans, lamprey, and rat. *Neuron, 24*(4), 809-817.

Koester, H. J., & Sakmann, B. (1998). Calcium dynamics in single spines during coincident pre- and postsynaptic activity depend on relative timing of back-

propagating action potentials and subthreshold excitatory postsynaptic potentials. *Proc Natl Acad Sci U S A, 95*(16), 9596-9601.

Kovalchuk, Y., Eilers, J., Lisman, J., & Konnerth, A. (2000). NMDA receptor-mediated subthreshold Ca(2+) signals in spines of hippocampal neurons. *J Neurosci, 20*(5), 1791-1799.

Legendy, C. R., & Salcman, M. (1985). Bursts and recurrences of bursts in the spike trains of spontaneously active striate cortex neurons. *J Neurophysiol, 53*(4), 926-939.

Li, Y. X., Zhang, Y., Lester, H. A., Schuman, E. M., & Davidson, N. (1998). Enhancement of neurotransmitter release induced by brain-derived neurotrophic factor in cultured hippocampal neurons. *J Neurosci, 18*(24), 10231-10240.

Liao, D., Zhang, X., O'Brien, R., Ehlers, M. D., & Huganir, R. L. (1999). Regulation of morphological postsynaptic silent synapses in developing hippocampal neurons. *Nat Neurosci, 2*(1), 37-43.

Lisman, J. (1989). A mechanism for the Hebb and the anti-Hebb processes underlying learning and memory. *Proc Natl Acad Sci U S A, 86*(23), 9574-9578.

Lisman, J. E. (1997). Bursts as a unit of neural information: making unreliable synapses reliable. *Trends Neurosci, 20*(1), 38-43.

Liu, G. (2004). Local structural balance and functional interaction of excitatory and inhibitory synapses in hippocampal dendrites. *Nat Neurosci, 7*(4), 373-379.

Lu, B. (2003). BDNF and activity-dependent synaptic modulation. *Learn Mem, 10*(2), 86-98.

Lu, H. C., Gonzalez, E., & Crair, M. C. (2001). Barrel cortex critical period plasticity is independent of changes in NMDA receptor subunit composition. *Neuron, 32*(4), 619-634.

Mackenzie, P. J., Umemiya, M., & Murphy, T. H. (1996). Ca2+ imaging of CNS axons in culture indicates reliable coupling between single action potentials and distal functional release sites. *Neuron, 16*(4), 783-795.

Mayer, M. L., & Westbrook, G. L. (1987). Permeation and block of N-methyl-D-aspartic acid receptor channels by divalent cations in mouse cultured central neurones. *J Physiol, 394*, 501-527.

Mayer, M. L., Westbrook, G. L., & Guthrie, P. B. (1984). Voltage-dependent block by Mg2+ of NMDA responses in spinal cord neurones. *Nature, 309*(5965), 261-263.

Murnick, J. G., Dube, G., Krupa, B., & Liu, G. (2002). High-resolution iontophoresis for single-synapse stimulation. *J Neurosci Methods, 116*(1), 65-75.

Murthy, V. N., Schikorski, T., Stevens, C. F., & Zhu, Y. (2001). Inactivity produces increases in neurotransmitter release and synapse size. *Neuron, 32*(4), 673-682.

Murthy, V. N., Sejnowski, T. J., & Stevens, C. F. (1997). Heterogeneous release properties of visualized individual hippocampal synapses. *Neuron, 18*(4), 599-612.

Murthy, V. N., & Stevens, C. F. (1998). Synaptic vesicles retain their identity through the endocytic cycle. *Nature, 392*(6675), 497-501.

Neher, E., & Sakmann, B. (1976). Single-channel currents recorded from membrane of denervated frog muscle fibers. *Nature, 260*(5554), 799-802.

Nishiyama, M., Hong, K., Mikoshiba, K., Poo, M. M., & Kato, K. (2000). Calcium stores regulate the polarity and input specificity of synaptic modification. *Nature, 408*(6812), 584-588.

Nowak, L., Bregestovski, P., Ascher, P., Herbet, A., & Prochiantz, A. (1984). Magnesium gates glutamate-activated channels in mouse central neurones. *Nature, 307*(5950), 462-465.

Philpot, B. D., Sekhar, A. K., Shouval, H. Z., & Bear, M. F. (2001). Visual experience and deprivation bidirectionally modify the composition and function of NMDA receptors in visual cortex. *Neuron, 29*(1), 157-169.

Philpot, B. D., Weisberg, M. P., Ramos, M. S., Sawtell, N. B., Tang, Y. P., Tsien, J. Z., et al. (2001). Effect of transgenic overexpression of NR2B on NMDA receptor function and synaptic plasticity in visual cortex. *Neuropharmacology, 41*(6), 762-770.

Poirazi, P., Brannon, T., & Mel, B. W. (2003). Pyramidal neuron as two-layer neural network. *Neuron, 37*(6), 989-999.

Polsky, A., Mel, B. W., & Schiller, J. (2004). Computational subunits in thin dendrites of pyramidal cells. *Nat Neurosci, 7*(6), 621-627.

Quinlan, E. M., Olstein, D. H., & Bear, M. F. (1999). Bidirectional, experience-dependent regulation of N-methyl-D-aspartate receptor subunit composition in the rat visual cortex during postnatal development. *Proc Natl Acad Sci U S A, 96*(22), 12876-12880.

Raastad, M., & Shepherd, G. M. (2003). Single-axon action potentials in the rat hippocampal cortex. *J Physiol, 548*(Pt 3), 745-752.

Rao, A., & Craig, A. M. (1997). Activity regulates the synaptic localization of the NMDA receptor in hippocampal neurons. *Neuron, 19*(4), 801-812.

Renger, J. J., Egles, C., & Liu, G. (2001). A developmental switch in neurotransmitter flux enhances synaptic efficacy by affecting AMPA receptor activation. *Neuron, 29*(2), 469-484.

Rowland, L. M., Astur, R. S., Jung, R. E., Bustillo, J. R., Lauriello, J., & Yeo, R. A. (2005). Selective cognitive impairments associated with NMDA receptor blockade in humans. *Neuropsychopharmacology, 30*(3), 633-639.

Ryan, T. A., Reuter, H., & Smith, S. J. (1997). Optical detection of a quantal presynaptic membrane turnover. *Nature, 388*(6641), 478-482.

Ryan, T. A., Reuter, H., Wendland, B., Schweizer, F. E., Tsien, R. W., & Smith, S. J. (1993). The kinetics of synaptic vesicle recycling measured at single presynaptic boutons. *Neuron, 11*(4), 713-724.

Ryan, T. A., & Smith, S. J. (1995). Vesicle pool mobilization during action potential firing at hippocampal synapses. *Neuron, 14*(5), 983-989.

Ryan, T. A., Smith, S. J., & Reuter, H. (1996). The timing of synaptic vesicle endocytosis. *Proc Natl Acad Sci U S A, 93*(11), 5567-5571.

Sabatini, B. L., Oertner, T. G., & Svoboda, K. (2002). The life cycle of Ca(2+) ions in dendritic spines. *Neuron, 33*(3), 439-452.

Schikorski, T., & Stevens, C. F. (1997). Quantitative ultrastructural analysis of hippocampal excitatory synapses. *J Neurosci, 17*(15), 5858-5867.

Schikorski, T., & Stevens, C. F. (2001). Morphological correlates of functionally defined synaptic vesicle populations. *Nat Neurosci, 4*(4), 391-395.

Shatz, C. J., & Stryker, M. P. (1988). Prenatal tetrodotoxin infusion blocks segregation of retinogeniculate afferents. *Science, 242*(4875), 87-89.

Shelton, D. L., Sutherland, J., Gripp, J., Camerato, T., Armanini, M. P., Phillips, H. S., et al. (1995). Human trks: molecular cloning, tissue distribution, and expression of extracellular domain immunoadhesins. *J Neurosci, 15*(1 Pt 2), 477-491.

Sheng, M., Cummings, J., Roldan, L. A., Jan, Y. N., & Jan, L. Y. (1994). Changing subunit composition of heteromeric NMDA receptors during development of rat cortex. *Nature, 368*(6467), 144-147.

Sircar, R., & Zukin, S. R. (1991). Kinetic mechanisms of glycine requirement for N-methyl-D-aspartate channel activation. *Brain Res, 556*(2), 280-284.

Slutsky, I., Sadeghpour, S., Li, B., & Liu, G. (2004a). Enhancement of synaptic plasticity through chronically reduced Ca2+ flux during uncorrelated activity. *Neuron, 44*(5), 835-849.

Slutsky, I., Sadeghpour, S., Li, B., & Liu, G. (2004b). Enhancement of Synaptic Plasticity through Chronically Reduced Ca(2+) Flux during Uncorrelated Activity. *Neuron, 44*(5), 835-849.

Stryker, M. P., & Harris, W. A. (1986). Binocular impulse blockade prevents the formation of ocular dominance columns in cat visual cortex. *J Neurosci, 6*(8), 2117-2133.

Tang, Y. P., Shimizu, E., Dube, G. R., Rampon, C., Kerchner, G. A., Zhuo, M., et al. (1999). Genetic enhancement of learning and memory in mice. *Nature, 401*(6748), 63-69.

Thiagarajan, T. C., Piedras-Renteria, E. S., & Tsien, R. W. (2002). alpha- and betaCaMKII. Inverse regulation by neuronal activity and opposing effects on synaptic strength. *Neuron, 36*(6), 1103-1114.

Timney, B., Mitchell, D. E., & Giffin, F. (1978). The development of vision in cats after extended periods of dark-rearing. *Exp Brain Res, 31*(4), 547-560.

Toescu, E. C., Verkhratsky, A., & Landfield, P. W. (2004). Ca2+ regulation and gene expression in normal brain aging. *Trends Neurosci, 27*(10), 614-620.

Tovar, K. R., Sprouffske, K., & Westbrook, G. L. (2000). Fast NMDA receptor-mediated synaptic currents in neurons from mice lacking the epsilon2 (NR2B) subunit. *J Neurophysiol, 83*(1), 616-620.

Tsien, J. Z., Huerta, P. T., & Tonegawa, S. (1996). The essential role of hippocampal CA1 NMDA receptor-dependent synaptic plasticity in spatial memory. *Cell, 87*(7), 1327-1338.

Turrigiano, G. G., Leslie, K. R., Desai, N. S., Rutherford, L. C., & Nelson, S. B. (1998). Activity-dependent scaling of quantal amplitude in neocortical neurons. *Nature, 391*(6670), 892-896.

Turrigiano, G. G., & Nelson, S. B. (2004). Homeostatic plasticity in the developing nervous system. *Nat Rev Neurosci, 5*(2), 97-107.

Vicini, S., Wang, J. F., Li, J. H., Zhu, W. J., Wang, Y. H., Luo, J. H., et al. (1998). Functional and pharmacological differences between recombinant N-methyl-D-aspartate receptors. *J Neurophysiol, 79*(2), 555-566.

Wallace, W., & Bear, M. F. (2004). A morphological correlate of synaptic scaling in visual cortex. *J Neurosci, 24*(31), 6928-6938.

Wang, X. J. (2001). Synaptic reverberation underlying mnemonic persistent activity. *Trends Neurosci, 24*(8), 455-463.

Watt, A. J., van Rossum, M. C., MacLeod, K. M., Nelson, S. B., & Turrigiano, G. G. (2000). Activity coregulates quantal AMPA and NMDA currents at neocortical synapses. *Neuron, 26*(3), 659-670.

Wiesel, T. N., & Hubel, D. H. (1963). Single-Cell Responses in Striate Cortex of Kittens Deprived of Vision in One Eye. *J Neurophysiol, 26*, 1003-1017.

Wong, H. K., Liu, X. B., Matos, M. F., Chan, S. F., Perez-Otano, I., Boysen, M., et al. (2002). Temporal and regional expression of NMDA receptor subunit NR3A in the mammalian brain. *J Comp Neurol, 450*(4), 303-317.

Woodbury, J., Lyons, K., Carretta, R., Hahn, A., & Sullivan, J. F. (1968). Cerebrospinal fluid and serum levels of magnesium, zinc, and calcium in man. *Neurology, 18*(7), 700-705.

Woodhull, A. M. (1973). Ionic blockage of sodium channels in nerve. *J Gen Physiol, 61*(6), 687-708.

Yuste, R., & Denk, W. (1995). Dendritic spines as basic functional units of neuronal integration. *Nature, 375*(6533), 682-684.

Zakharenko, S. S., Patterson, S. L., Dragatsis, I., Zeitlin, S. O., Siegelbaum, S. A., Kandel, E. R., et al. (2003). Presynaptic BDNF required for a presynaptic but not postsynaptic component of LTP at hippocampal CA1-CA3 synapses. *Neuron, 39*(6), 975-990.

Zakharenko, S. S., Zablow, L., & Siegelbaum, S. A. (2001). Visualization of changes in presynaptic function during long-term synaptic plasticity. *Nat Neurosci, 4*(7), 711-717.